Global O₃-CO Correlations in a Chemistry and Transport Model during July–August: Evaluation with TES Satellite Observations and Sensitivity to Input Meteorological Data and Emissions

Hyun-Deok Choi[1], Hongyu Liu[1], James H. Crawford[2], David B. Considine[2,3], Dale J. Allen[4], Bryan N. Duncan[5], Larry W. Horowitz[6], Jose M. Rodriguez[5], Susan E. Strahan[5,7], Lin Zhang[8,9], Xiong Liu[8], Megan R. Damon[5,10], and Stephen D. Steenrod[5,7]

[1]National Institute of Aerospace, Hampton, VA
[2]NASA Langley Research Center, Hampton, VA
[3]Now at NASA Headquarters, Washington, D.C.
[4]University of Maryland, College Park, MD
[5]NASA Goddard Space Flight Center, Greenbelt, MD
[6]NOAA Geophysical Fluid Dynamics Laboratory, Princeton, NJ
[7]Universities Space Research Association, Columbia, MD
[8]Harvard University, Cambridge, MA
[9]Now at Peking University, Beijing, China
[10]Science Systems and Applications, Inc., Lanham, MD

Atmos. Chem. Phys., revised, May 2017

Correspondence:

Hongyu Liu

Chemistry and Dynamics Branch, Mail Stop 401B

NASA Langley Research Center, Hampton, VA 23681

Tel: 757-864-3191; Email: Hongyu.Liu-1@nasa.gov

Abstract. We examine the capability of the Global Modeling Initiative (GMI) chemistry and transport model to reproduce global mid-tropospheric (618hPa) O_3-CO correlations determined by the measurements from Tropospheric Emission Spectrometer (TES) aboard NASA's Aura satellite during boreal summer (July–August). The model is driven by three meteorological data sets (fvGCM with sea surface temperature for 1995, GEOS4-DAS for 2005, and MERRA for 2005), allowing us to examine the sensitivity of model O_3-CO correlations to input meteorological data. Model simulations of radionuclide tracers (^{222}Rn, ^{210}Pb, and ^{7}Be) are used to illustrate the differences in transport-related processes among the meteorological data sets. Simulated O_3 values are evaluated with climatological ozone profiles from ozonesonde measurements and satellite tropospheric O_3 columns. Despite the fact that the three simulations show significantly different global and regional distributions of O_3 and CO concentrations, they show similar patterns of O_3-CO correlations on a global scale. All model simulations sampled along the TES orbit track capture the observed positive O_3-CO correlations in the Northern Hemisphere mid-latitude continental outflow and the Southern Hemisphere subtropics. While all simulations show strong negative correlations over the Tibetan Plateau, northern Africa, northern subtropical eastern Pacific, and Caribbean, TES O_3 and CO concentrations at 618 hPa only show weak negative correlations over much narrower areas (i.e., the Tibetan Plateau and northern Africa). Discrepancies in regional O_3-CO correlation patterns in the three simulations may be attributed to differences in convective transport, stratospheric influence, and subsidence, among other processes. To understand how various emissions drive global O_3-CO correlation patterns, we examine the sensitivity of GMI/MERRA model-calculated O_3 and CO concentrations and their correlations to emission types (fossil fuel, biomass burning, biogenic, and lightning NO_x emissions). Fossil fuel and biomass burning emissions are mainly responsible for the strong positive O_3-CO correlations over

continental outflow regions in both hemispheres. Biogenic emissions have a relatively smaller impact on O_3-CO correlations than other emissions, but are largely responsible for the negative correlations over the tropical eastern Pacific, reflecting the fact that O_3 is consumed and CO generated during the atmospheric oxidation process of isoprene under low NO_x conditions. We find that lightning NO_x emissions degrade both positive correlations at mid-/high- latitudes and negative correlations in the tropics because ozone production downwind of lightning NO_x emissions is not directly related to the emission and transport of CO. Our study concludes that O_3-CO correlations may be used effectively to constrain the sources of regional tropospheric O_3 in global 3-D models, especially for those regions where convective transport of pollution plays an important role.

1. Introduction

Ozone (O_3) is an important greenhouse gas in the troposphere and a pollutant at the surface. It is a primary source of the hydroxyl radical (OH), which controls the oxidizing power of the troposphere. Ozone in the troposphere is produced by photochemical oxidation of carbon monoxide (CO), methane, and volatile organic hydrocarbons (VOCs) in the presence of nitrogen oxides ($NO_x \equiv NO + NO_2$). Its precursors are emitted by human activity (e.g., fossil fuel combustion and industrial processes), biomass burning, vegetation, soils, and lightning. Ozone is also transported down from the stratosphere by the Brewer Dobson circulation. Carbon monoxide is a product of incomplete combustion. Its sources include fossil fuel and biofuel combustion, biomass burning, and chemical production from atmospheric oxidation of methane, isoprene, and other VOCs. Its primary sink is reaction with OH.

1   Since CO is a precursor of tropospheric O_3 and an excellent tracer for long-range transport

2   of pollution owing to its tropospheric lifetime of a few months, correlations between O_3 and CO

3   are useful indicators of the efficiency of O_3 production and export (e.g., Parrish et al., 1993; Mao

4   and Talbot, 2004). Generally, a positive correlation in summer indicates strong photochemical

5   production of O_3 downwind of polluted regions (Chin et al., 1994; Tsutsumi and Matsueda, 2000).

6   A negative correlation indicates stratospheric influence (Parrish et al., 1998; Hsu et al., 2004),

7   photochemical O_3 destruction (Fishman and Seiler, 1983; Parrish et al., 1998; Mao and Talbot,

8   2004), or chemical production of CO (Chin et al., 1994; Real et al., 2008). Small correlation

9   coefficients and small linear regression slopes are indications of fresh pollution plumes that have

10   not yet realized their O_3 production potential due to, for example, incomplete photochemical

11   processes (Naja et al., 2003).

12   Many studies have used surface and/or aircraft observed O_3-CO correlations to understand

13   anthropogenic influences on O_3, especially in the Northern Hemisphere (NH) continental outflow

14   regions such as the northeastern US/northern Atlantic (Fishman and Seiler, 1983; Anderson et al.,

15   1993; Parrish et al., 1993; Chin et al., 1994; Fehsenfeld et al., 1996; Parrish et al., 1998; Li et al.,

16   2002; Honrath et al., 2004; Mao and Talbot, 2004) and the Asian Pacific Rim (Tsutsumi and

17   Matsueda, 2000; Mauzerall et al., 2000). The studies found strong O_3-CO correlations in outflow

18   regions and concluded that the export of pollution from the NH major continents makes a

19   significant contribution to total tropospheric O_3 over the NH during summer.

20   The observed O_3-CO correlation coefficients and linear regression slopes have been used

21   to evaluate the capability of models of chemistry and transport to produce proper O_3 levels from

22   its precursors for the right reasons (e.g., Chin et al., 1994; Mauzerall et al., 2000; Zhang et al.,

23   2006; Voulgarakis et al., 2011). Shim et al. (2009) examined the Mexico City pollution outflow

using O_3, CO, and their correlations from TES as well as aircraft measurements obtained during the Megacity Initiative: Local and Global Research Observations (MILAGRO) / Intercontinental Chemical Transport Experiment (INTEX-B) campaigns. These investigations found that TES data is characterized by smaller O_3-CO correlation coefficients but larger linear regression slopes than *in situ* observations at 618 hPa partly due to the lack of variability in TES CO. Two previous studies also examined TES global O_3-CO correlations. Zhang et al. (2006) compared mid-tropospheric TES O_3-CO correlations in July 2005 over the eastern United States with those from the GEOS-Chem model and International Consortium for Atmospheric Research on Transport and Transformation (ICARTT) aircraft observations (July 2004), finding that TES can provide good information on global mid-tropospheric O_3-CO correlations. Voulgarakis et al. (2011) expanded the scope of Zhang et al. (2006), evaluating O_3-CO correlations simulated by two independent models against five years of TES observations. They suggested that in addition to O_3 photochemical processes, transport may also play an important role in the O_3-CO correlations. However, Voulgarakis et al. (2011) could not isolate the effect of transport because the two models in their study used different input meteorological data sets as well as different chemical and transport mechanisms.

In this paper, we present O_3 and CO simulations using the Global Modeling Initiative (GMI) chemistry and transport model (CTM) driven by three meteorological data sets. The model can incorporate different inputs and components (e.g., meteorological fields, emission inventories, and chemical mechanisms), allowing us to test the sensitivity of model simulations to input meteorological data sets (e.g., Douglass et al., 1999; Considine et al., 2005; Liu et al., 2016). Model simulations are evaluated using ozonesonde and satellite observations. We then test the model's capability to reproduce the mid-tropospheric O_3-CO correlations determined from TES

measurements. We present the differences in the simulated O_3-CO correlations due to the use of different meteorological input data, and interpret those differences in terms of transport using radionuclide species (^{222}Rn, ^{210}Pb, and ^{7}Be) as tracers of atmospheric transport (see Section 2.1.3). We also investigate the effect of emission types on O_3 and CO concentrations and their correlations in the model.

This paper is organized as follows. Section 2: Descriptions of the GMI model, meteorological data sets, and observational data sets. Section 3: Presentation of the model simulations of radionuclides, O_3 and CO. Section 4: Evaluation of GMI O_3 and CO simulations with observations. Section 5: Evaluation of GMI O_3-CO correlations with satellite observations from TES. Section 6: Analysis of the effects of various emission types on the model simulated O_3-CO correlations. Section 7: Summary and conclusions.

2. Model and Data

2.1. GMI

2.1.1. The CTM

The GMI CTM is a global 3-D composition model that combines both tropospheric and stratospheric chemical mechanisms, including 124 species, 322 chemical reactions, and 81 photolysis reactions (Ziemke et al, 2006; Duncan et al., 2007a; Considine et al., 2008; Allen et al., 2010). The tropospheric mechanism includes a detailed description of tropospheric O_3-NOx-hydrocarbon chemistry (Bey et al., 2001) with recent updates (e.g., see Allen et al., 2010). The stratospheric mechanism is described in Kinnison et al. (2001) and Douglass et al. (2004). The

1   details of the GMI model are described in Duncan et al. (2007a) and Strahan et al. (2007). The

2   basic structure of the model is described in Rotman et al. (2001).

3   The GMI model uses a flux-form semi-Lagrangian (FFSL) advection scheme (Lin and

4   Rood, 1996) and also includes parameterizations of convection, wet scavenging, dry deposition,

5   and planetary boundary layer mixing. The anthropogenic emission (e.g., fossil fuel emissions)

6   scheme is from Bey et al. (2001), Benkovitz et al. (1996), and Duncan et al. (2007b). We use the

7   anthropogenic emission inputs for 2005 for all simulations in this study. The biogenic emission

8   scheme is calculated online based on Guenther et al. (2006) and biofuel emissions are estimated

9   from the inventory and emission factors of Yevich and Logan (2003). Biomass burning emissions

10   are from Duncan et al. (2003) climatology, where the spatial and seasonal variability are derived

11   from satellite observations of monthly total fire counts. Lightning NO_x emissions are calculated

12   locally in deep convection events with the scheme of Allen et al. (2010) where flash rates are

13   assumed to be proportional to the square of upward convective mass flux but constrained by

14   monthly average climatological flash rates from V2.2 of the Optical Transient Detector and the

15   Lightning Imaging Sensor (OTD/LIS) climatology. GMI uses modules developed at Harvard

16   University to calculate wet scavenging (Mari et al., 2000; Liu et al., 2001) and dry deposition rates

17   (Jacob and Wofsy, 1990).

18   Several studies have previously evaluated the GMI CTM simulations of tropospheric O_3

19   and CO. Ziemke et al. (2006) compared the tropospheric ozone columns (TOC) in an earlier

20   version of the GMI CTM, which was driven by the fvGCM meteorological fields (details in Section

21   2.1.2), with those determined from Ozone Monitoring Instrument/Microwave Limb Sounder

22   (OMI/MLS) measurements from the NASA Aura satellite. The comparison showed similarities

23   with respect to zonal and seasonal variations of TOC, but the model overestimated TOC over

northern Africa by as much as 10 DU, likely due to desert dust effects while underestimating TOC

over the western Pacific warm pool by up to 10 DU. Chandra et al. (2009) evaluated GMI TOC

when driven by the GEOS4 meteorological fields (see Section 2.1.2) with OMI/MLS TOC and

found the model overestimated TOC by 5-10 DU for the latitude band 30°N - 35°N all the year

and over east China in winter and spring when stratosphere-troposphere exchange (STE) is greatest.

Duncan et al. (2008) showed that the annual average surface O_3 concentrations in the GMI/GEOS4

simulation had a high bias of about 11%, with higher biases in summer when photochemical

production is the dominant source of O_3. Considine et al. (2008) examined the ability of

GMI/fvGCM ($4° \times 5°$) to represent the observed near-tropopause O_3 distributions and found that

annual mean O_3 concentrations were biased high by 45% at the model thermal tropopause likely

due to insufficient vertical resolution near the tropopause (~ 1.1 km) and/or too high vertical

diffusivity.

For CO, Duncan et al. (2007a) compared GMI/fvGCM simulated tropospheric CO

concentrations with NOAA Global Monitoring Division (GMD) surface observations. They

showed that the model was biased low at most sites in local winter/spring likely due to

overestimation of OH in the simulation when the CO burden is typically at an annual maximum.

Schoeberl et al. (2006) showed that GMI/fvGCM was able to reproduce the upper

troposphere/lower stratosphere (UT/LS) CO tape recorder caused by seasonal changes in biomass

burning, as identified with the MLS data.

2.1.2. fvGCM, GEOS4, and MERRA Meteorological Data Sets

We drive the GMI CTM with three meteorological datasets from: the free-running NASA

Global Modeling and Assimilation Office (GMAO) finite-volume General Circulation Model

(fvGCM with sea surface temperature for 1995), the Goddard Earth Observing System Data Assimilation System Version 4 (GEOS4-DAS) for 2005, and the Modern-Era Retrospective Analysis for Research and Applications (MERRA) for 2005. Note that the fvGCM is the general circulation model in the assimilation system used to generate GEOS4-DAS (Bloom et al., 2005). The native vertical coordinate of fvGCM and GEOS4-DAS models is a generalized hybrid sigma-pressure coordinate system with 55 vertical layers and a smooth transition between sigma in the troposphere (pressure > 200 hPa) and pure pressure in the stratosphere (top pressure 0.01 hPa). MERRA is a NASA atmospheric reanalysis data set from a new version of GEOS-DAS Version 5 (GEOS-5.2.0). GEOS-5 is a system of models integrated using the Earth System Modeling Framework (ESMF). Compared to GEOS-4, GEOS-5 adopts an analysis system developed jointly with the National Centers for Environmental Prediction (NCEP) and a different set of physics packages for the atmospheric GCM. MERRA has 72 vertical levels with a lid at 0.01 hPa (sigma-pressure coordinate interface at ~177 hPa). The native horizontal resolution of all meteorological data sets is $1° \times 1.25°$. To improve computational efficiency, we drive GMI CTM with the meteorological data sets at a degraded resolution (2° latitude by 2.5° longitude). All standard and perturbation full-chemistry simulations for July-August as presented in this paper were conducted with a 6-month spinup.

The different convective parameterizations used to generate the meteorological data sets alters the characteristics of convective transport of chemical species. Both fvGCM and GEOS4 use the deep convection scheme of Zhang and McFarlane (1995) and the shallow convection scheme of Hack (1994) whereas MERRA uses a modified version of the Relaxed Arakawa-Schubert scheme for convection (Moorthi and Suarez, 1992). Figure 1 shows the latitude-pressure cross sections of zonal mean convective mass fluxes averaged over three meteorological data fields

and the differences from the average during July – August. fvGCM shows the strongest shallow

convection in the Southern Hemisphere (SH) mid- and low-latitudes among the models. GEOS4

shows the strongest convection in the tropical middle troposphere. MERRA is characterized by

the weakest shallow convection in both hemispheres. MERRA has the strongest tropical

convection in the lower free troposphere, but its tropical convection is not as deep as in the others.

Shallow convection in fvGCM and GEOS4 extends to higher latitudes compared to MERRA.

2.1.3. Radionuclide Tracers

We conduct GMI model simulations of radionuclides (^{222}Rn, ^{210}Pb, and ^{7}Be) to examine

the relative effects of convection, stratospheric influence, and large-scale subsidence on the

transport of trace species and their sensitivity to input meteorological data sets. ^{222}Rn has a half-

life of 3.8 days and is emitted primarily from continental crust. It is useful as a tracer of convective

transport in global models (e.g., Jacob et al., 1997). ^{210}Pb, a decay daughter of ^{222}Rn, has a

radioactive half-life of 22.3 years, and ^{7}Be, which is produced by cosmic ray spallation reactions

in the stratosphere and UT, has a radioactive half-life of 53.3 days. Because ^{210}Pb and ^{7}Be attach

to submicron aerosols after production and are therefore scavenged by precipitation or deposited

to the surface, they have been used as a pair to test wet deposition schemes in global models (e.g.,

Liu et al., 2001). ^{7}Be is also used as a tracer for STE (Dibb et al., 1994; Liu et al., 2001; Liu et al.,

2016). The ratio ^{7}Be/^{210}Pb is useful as an indicator of vertical transport because the ratio is

insensitive to precipitation scavenging (Koch et al., 1996). All simulations of radionuclide tracers

were conducted with a 5-year spinup in order for ^{210}Pb to reach an equilibrium in the stratosphere.

2.2. Data Sets

2.2.1. Ozonesonde O$_3$

1   We use climatological ozone profiles from 23 ozonesonde stations averaged over July –

2   August from 1985 to 2000, originally constructed by Considine et al. (2008) based on Logan (1999)

3   and Thompson et al. (2003). The number of soundings at each station is adequate for defining

4   monthly means used to evaluate the accuracy of the model results (Considine et al., 2008; Liu et

5   al., 2016).

6   **2.2.2. Satellite Tropospheric Ozone Column (TOC)**

7   Three TOC products are used in this study: Total Ozone Mapping Spectrometer (TOMS)

8   – Solar Backscatter Ultraviolet (SBUV), OMI-MLS, and directly retrieved TOC from TES. The

9   TOMS-SBUV TOC and OMI-MLS TOC are determined using the tropospheric ozone residual

10   (TOR) method, which involves subtracting measurements of SBUV and MLS stratospheric

11   column ozone (SCO) from TOMS and OMI total column ozone, respectively (Fishman et al., 2003;

12   Ziemke et al., 2006). The TES TOCs are integrated from directly retrieved volume mixing ratios.

13   We did not consider different instrument sensitivities because integrating retrievals significantly

14   reduces the error due to averaging over pressure ranges larger than TES vertical resolution

15   (Osterman et al., 2008; Zhang et al., 2012). The tropopause pressure is taken from the GEOS4

16   meteorological data (2° x 2.5°). A description of TES retrievals is given in Section 2.2.3.

17   **2.2.3. TES O_3 and CO.**

18   The TES instrument on EOS-Aura routinely provides observations of tropospheric O_3 and

19   CO across the globe (Beer et al., 2001; Beer, 2006). The Aura satellite is on a polar sun-

20   synchronous orbit with equator crossing at 01:45 (descending) and 13:45 (ascending) local time.

21   TES is a Fourier transform infrared emission spectrometer with high spectral resolution (0.1 cm^{-1})

22   and wide spectral range (650 – 3050 cm^{-1}) (Beer et al., 2001). The nadir footprint of TES is 5×8

km. TES observations consist of two modes: global survey and special observations (Beer et al., 2001). We use TES level 2, version 4 global survey nadir observations (http://eosweb.larc.nasa.gov/) and only O_3 and CO retrievals with the "Master" quality flag are used in this analysis. The retrievals of O_3 have $1 - 1.5$ degrees of freedom (DOF) in the profile at mid-latitudes in summer, with peak sensitivities near 700 hPa and 300-400 hPa, respectively (Parrington et al., 2008). TES CO profiles generally have $1 - 1.5$ DOFs in the troposphere (Luo et al., 2007ab). Detailed descriptions of the TES instrument and the O_3 and CO retrieval algorithms are described in Beer et al. (2001, 2006), Worden et al. (2004), and Bowman et al. (2002, 2006).

In this study, we use O_3 and CO retrievals at 618 hPa level, where TES has good sensitivity for both O_3 and CO centered in the MT, and exclude latitudes $> 60°$ where TES measurements are less reliable due to low brightness temperatures (Zhang et al., 2006). Due to limitation of TES vertical resolution ($1 - 1.5$ DOFs in the troposphere for both O_3 and CO), TES averaging kernels are applied to the simulations to take into account the different sensitivities of the instruments. TES uses MOZART model output binned by month and in blocks of 10° latitude by 60° longitude as a priori profiles (Worden et al., 2004). Validation of TES O_3 against ozonesondes showed that TES ozone typically has a high bias of about 10% in the UT (Worden et al., 2007) or 3-10 ppbv in the MT/UT (Nassar et al., 2008). TES CO has a negative bias (<10%) compared to aircraft measurements in the NH mid-latitude LT/MT during the INTEX-B mission (spring 2006) (Luo et al., 2007a).

3. Model Simulations of Radionuclides, O_3, and CO

3.1. GMI Simulations of Radionuclides

1   Figures 2 and 3 show the latitude-pressure cross sections of zonal mean concentrations of

2   ^{222}Rn and stratospheric fraction (%) of tropospheric ^{7}Be concentrations during July – August for

3   the values averaged over three meteorological data sets and the differences from the mean.

4   Differences in zonal mean ^{222}Rn concentrations at SH mid-latitudes among the three simulations

5   are small despite much stronger shallow convection in fvGCM (Figure 1). This reflects the fact

6   that most convection at SH mid-latitudes occurs over the ocean. However, GMI/fvGCM ^{222}Rn

7   concentrations in the UT at NH subtropics and mid-latitudes are ~ 20 – 70 % higher than those in

8   other simulations due to the deeper convection in fvGCM (Figure 1). In the tropical UT/MT,

9   GMI/MERRA produced the lowest ^{222}Rn concentrations, consistent with the lower cutoff of

10 convection in GMI/MERRA (Figure 2). This is not inconsistent with the largest stratospheric

11 influence in the tropical UT/MT in GMI/MERRA among the three meteorological data sets (Figure

12 3). Previously, Liu et al. (2010) and Zhang et al. (2011) used GEOS-Chem simulations of CO and

13 ^{222}Rn (driven by GEOS4 DAS and GEOS5 DAS meteorological data) to show that the tropical

14 convection in GEOS4 is deeper than in GEOS5. Because the MERRA reanalysis utilizes the same

15 GCM as the GEOS5 DAS, it also utilizes the Relaxed Arakawa-Schubert (RAS) convection.

16   The stratospheric contribution to the lower-tropospheric ^{7}Be concentrations in

17 GMI/fvGCM peaks near 30 - 75°N (20 – 25%), in contrast to the GMI/GEOS4 and GMI/MERRA

18 simulations (Figure 3). The GMI/GEOS4 and GMI/MERRA simulations show a similar pattern of

19 stratospheric influence on the troposphere with maxima near 0 – 30°S and >30°S (20 - 30%),

20 respectively, in the LT. However, GMI/GEOS4 suggests more stratospheric influence than

21 GMI/MERRA in the MT near 30°S (30 - 35%) and near 30 – 45°N (~ 25%). The stratospheric

22 impacts on the tropical MT/UT are weakest in GMI/fvGCM and strongest in GMI/MERRA. At

23 NH mid-latitudes, stratospheric influences on the LT are largest and most extensive in

GMI/fvGCM and smallest in GMI/MERRA. These differences in stratospheric influence that characterize these meteorological data sets will be used to interpret GMI O_3 and CO simulations driven by these meteorological fields (Sections 3.2 and 4).

3.2. GMI Simulations of O_3 and CO

Figures 4-5 show the latitude-pressure cross sections of zonal mean mixing ratios of O_3 and CO during July – August averaged over three simulations and the differences from the mean. The latitudinal distributions of O_3 from all simulations show lowest O_3 concentrations near the surface at high latitudes and in the tropical LT (Figure 4). Relatively low O_3 in the tropical free troposphere results from transport of ozone-poor air from the LT to UT/MT via deep convection. High O_3 concentrations are seen in the (subtropical) descending branches of the Hadley circulation partly due to the influence of STE. Compared with GMI GEOS4 and GMI/MERRA, GMI/fvGCM simulates higher O_3 in the NH mid-latitude MT and lower O_3 in the SH LT/MT. This is likely due to higher STE in the NH and weaker STE in the SH, respectively, as suggested by the higher (lower) fraction of stratospheric [7]Be seen in the GMI/fvGCM simulation compared to the other two simulations (Figure 3). On the other hand, GMI/MERRA simulates the highest O_3 in the tropical MT/UT as a result of "stronger but shallower" deep convection in the tropics (Figure 1). All simulations show the largest CO concentrations in the tropical LT/MT and NH mid-latitude boundary layer (Figure 5). The former reflects convective lifting of tropical biomass burning CO emissions and the latter anthropogenic CO emissions, respectively. Among the three simulations, GMI/fvGCM simulates the lowest CO concentrations in the tropical MT/UT as well as both hemispheres. In the NH MT/UT in GMI/fvGCM, the low CO concentrations result from high OH concentrations associated with high O_3 concentrations due to higher STE, which will be discussed in Section 4.1. In the SH GMI/fvGCM, the low CO concentrations are due to high OH

concentrations as a result of too low NO_x emissions from lightning (see Section 4.1). Tropical

MT/UT CO concentrations in GMI/MERRA are not as high as those in GMI/GEOS4, again

reflecting the "shallower" tropical deep convection in MERRA.

4. Evaluation of GMI O_3 and CO Simulations with Observations

In this section, we evaluate GMI O_3 and CO simulations driven by the fvGCM, GEOS4,

and MERRA meteorological data sets with ozonesonde O_3 vertical profiles, satellite TOC, and

TES O_3 and CO retrievals.

4.1. Ozone Vertical Profiles and Tropospheric Ozone Column

Figure 6 compares GMI simulated tropospheric O_3 profiles with ozonesonde observations

averaged over July-August for a range of latitudes. These results are typical of other stations at

similar latitudes. The mean differences between simulated O_3 and ozonesonde observations at 500

hPa (MT) and 200 hPa (UT), respectively, are listed in Table 2. GMI/fvGCM overestimates O_3 in

the NH high-/mid-latitude UT/MT (e.g., Churchil, Hohenpeissenberg, and Sapporo). This may be

due to excessive STE given the relatively high fractions of ^{7}Be from the stratosphere (Figure 3).

The overestimate may also be partly attributed to strong convective mass fluxes in the NH mid-

latitude that lift more O_3 and/or its precursors from the surface (Figures 1-2). Figure 6 also shows

that GMI/fvGCM underestimates O_3 in the SH (e.g., Reunion Island). Since stratospheric ^{7}Be

fractions are relatively low in this simulation, the O_3 underestimate may be due to overly weak

STE (cf. Figure 3). Low emissions of lightning NO_x, an important precursor of tropospheric O_3

could also play a role. It is noted that all simulations show hot spots of LNO_x emissions over the central

and eastern US, central Africa, and west Tibetan plateau (not shown). Lightning NO_x emissions between

1   10°S and 70°S in GMI/fvGCM during July-August are similar to those in GMI/GEOS4 and

2   GMI/MERRA, but the emissions during May-June are a factor of ~ 2.5 lower than those in

3   GMI/GEOS4 and GMI/MERRA (Table 1). Since O_3 has a lifetime of weeks to months in the

4   UT/MT, a low-O_3 bias during May-June will lead to lower O_3 during July-August in GMI/fvGCM.

5   GMI/GEOS4 simulates O_3 in both hemispheres reasonably well but underestimates O_3 in the

6   tropical UT/MT, as seen at Paramaribo and Nairobi in Figure 6. GMI/MERRA underestimates O_3

7   in the NH high-latitude UT (e.g., Resolute) likely due to weak STE compared to GMI/GEOS4 as

8   suggested by [7]Be tracer simulations (Figure 3), while it overestimates O_3 with a high bias in the

9   SH subtropics (e.g., Samoa and Reunion Island) because of a combination of excessive influences

10   from lightning NO_x emissions in May (Table 1) and STE (or subsidence from UT) (Figure 3). In

11   addition, the shallower tropical convection (Figure 1) accompanied by larger STE contribution in

12   the southern tropical MT/UT (Figure 3) results in less clean air being lifted from the LT to MT/UT.

13   Figure 7 shows GMI simulated zonal mean TOCs averaged over July – August in

14   comparison with TORs determined from TOMS/SBUV (Fishman et al., 2003), OMI/MLS

15   (Ziemke et al., 2006), and TOCs directly retrieved from TES measurements. The World

16   Meteorological Organization (WMO) definition of thermal tropopause is used to calculate the

17   model TOC, following Liu et al. (2016). The latitudinal distribution of TOCs shows a trough in

18   the tropics and polar regions, and a peak at mid-latitudes in both the models and the observations.

19   The TORs determined from TOMS/SBUV and OMI/MLS agree well with each other in the NH,

20   but those from OMI/MLS are lower at ~10ºN and higher at south of 50ºS. The TOCs determined

21   from TES are more similar to the OMI/MLS TORs, but biased high in the northern subtropics, and

22   biased low at south of 40ºS. A comparison of Figure 7 with Figure 6 indicates that the TOCs from

23   three model simulations coincide with the above results from model evaluations with ozonesonde

O$_3$ profiles. For example, both evaluations suggest negative biases in the SH and positive biases in the NH high-/mid-latitudes in GMI/fvGCM, and positive biases in the southern subtropics in GMI/MERRA.

4.2. O$_3$ and CO Concentrations at 618 hPa

Figure 8 shows the July-August mean concentrations of O$_3$ and CO at 618 hPa in the GMI simulations. Figure 9 shows the corresponding global distributions of ^{222}Rn concentrations, stratospheric fractions (%) of mean tropospheric ^{7}Be concentrations, and ratios ^{7}Be/^{210}Pb. All simulations show highest O$_3$ concentrations at NH mid-latitudes and lowest O$_3$ concentrations in the tropical western Pacific. They also simulate a narrow band of relatively high O$_3$ concentrations in the southern tropics and subtropics. GMI/fvGCM simulates highest O$_3$ concentrations at NH mid/high latitudes (Figure 8, left panel) likely due to STE, as indicated by a large fraction of ^{7}Be transported down from the stratosphere (Figure 9, middle top panel). By contrast, it simulates the lowest O$_3$ concentrations in the southern tropics and subtropics, especially over southern Africa and South Atlantic Ocean. In this region, GMI/MERRA simulates the highest O$_3$ concentrations attributed to high lightning NO$_x$ emissions (Table 1), large STE (Figure 9, middle bottom panel), and biomass burning emissions lifted by shallow but strong convection (Section 3; Figure 9, left bottom panel). Thompson et al. (1996) previously suggested that the O$_3$ maximum observed in southern Africa and the adjacent Atlantic during September - October 1992 is caused by the coincidence of O$_3$ precursors from biomass burning with long residence time, and deep convection with additional lightning NO$_x$ and biogenic sources. As we will show in Section 5, the emission types contributing to the O$_3$ enhancements over this region in July – August mainly include lightning NO$_x$ and, to a lesser extent, biomass burning.

1    All simulations show a similar pattern of CO concentrations at 618 hPa, e.g., CO

2  enhancements due to biomass burning emissions lifted by convection (e.g., South America, Africa,

3  Indonesia, and Alaska) and anthropogenic emissions (e.g., East Asia, South Asia, and eastern

4  North America) (Figure 8, right column). This pattern also reflects the geographic distribution of

5  these emissions. GMI/fvGCM simulates lowest CO concentrations at 618 hPa in most of the

6  polluted regions due to stronger STE of O_3, as discussed in Section 4.1. GMI/GEOS4 simulates

7  slightly lower CO concentrations in East and South Asia, North America and their outflow regions,

8  and Indonesia than GMI/MERRA does. GMI/GEOS4 also simulates lower CO concentrations over

9  subtropical South American and African westerly outflow regions.

10    To evaluate GMI O_3 and CO simulations with satellite observations, we use TES retrievals

11  at 618 hPa where TES has good sensitivity for both O_3 and CO in the MT (Zhang et al., 2006).

12  GMI model output was sampled along the TES orbit track at the observation time and then

13  interpolated onto the 67 vertical pressure levels of TES retrievals. Since the model output was

14  saved every 3 hours, the temporal offset with TES is up to 1.5 hours. To compare the model output

15  with the TES retrieved profiles, TES averaging kernels and *a priori* were applied to the model

16  output. Both the model output and TES data were gridded onto grids of 10° latitude by 10°

17  longitude by averaging all values within each grid box. Figures 10-11 show the mean

18  concentrations of O_3 and CO at 618 hPa observed by TES during July - August 2005 and

19  corresponding GMI CTM results.

20    TES observed enhanced O_3 concentrations over the Middle East, northern Africa, southern

21  Africa, North America, and East Asia (Figure 10). Increased levels of O_3 were also observed in

22  continental outflow regions, especially the northwestern Pacific, North Atlantic, tropical south

23  Atlantic, and southern subtropical Indian Ocean. All simulations capture the spatial distributions

of O_3 well but underestimate the enhancements over southern Africa and adjacent oceans. GMI/fvGCM simulates reasonably well the TES-observed O_3 enhancements at NH mid/high latitudes but slightly underestimates the low O_3 concentrations in the tropical western Pacific and Indian Ocean. GMI/GEOS4 and GMI/MERRA simulations show lower O_3 concentrations at NH mid/high latitudes compared to TES observations. However, considering that TES O_3 has a positive bias of 3-10 ppbv in the MT (Nassar et al., 2008), GMI/fvGCM may very well overestimate O_3 at NH mid-latitudes while GMI/GEOS4 and GMI/MERRA simulations are closer to reality. This conclusion is consistent with that from the comparison of GMI simulations with ozonesonde observations (Figure 6).

Enhanced CO concentrations were observed by TES over Africa, South America, North America, and Eurasia (Figure 11). All simulations underestimated CO concentrations in most of those CO hot spots in the NH. GMI/GEOS4 captured fairly well high CO concentrations over biomass burning regions in South America and Africa. However, considering TES CO biases, i.e., a negative bias at NH mid-latitudes and a positive bias in the tropics (Luo et al., 2007a; Lopez et al., 2008), all simulations significantly underestimate CO enhancements at NH mid-latitudes but simulate better CO enhancements over the tropical biomass burning regions. This is consistent with a previous study by Shindell et al. (2006) who found a multi-model underestimate of NH extratropical CO likely due to current inventories underestimating fossil fuel emissions in East Asia and biomass burning emissions in south-central Africa.

5. O_3 and CO Relationships

In this section, we examine O_3 and CO relationships at 618hPa in GMI CTM. We interpret GMI simulated O_3-CO correlations and their slopes in the context of emissions, photochemical transformation, and transport (e.g., convection, STE, and large-scale subsidence), using model meteorological data and radionuclide simulations. We then evaluate them with those derived from TES satellite observations. Note that the model underestimate of CO concentrations does not significantly affect the calculated O_3-CO correlations although it may cause biases in the regression slopes due to the association of the latter with ozone production efficiency.

5.1. GMI O_3-CO Correlations

Figure 12 shows the O_3-CO correlation coefficients (R) and linear regression slopes (dO_3/dCO) at 618 hPa for July – August, as calculated using the reduced major axis method with 3-hourly output from the GMI/fvGCM, GMI/GEOS4, and GMI/MERRA simulations. We discuss the common features in the correlation patterns in all simulations, followed by their discrepancies. All simulations show strong positive O_3-CO correlations and large dO_3/dCO enhancement ratios in the NH major continental outflow regions, e.g., Atlantic Seaboard, northern Atlantic, and northern Pacific, consistent with previous modeling studies (Zhang et al., 2006; Voulgarakis et al., 2011) and in situ observations (e.g., Anderson et al. 1993; Chin et al., 1994; Jaffe et al., 1996; Parrish et al., 1998; Tsutsumi and Matsueda, 2000; Mao and Talbot, 2004). Our simulations also suggest a much larger area with high correlations that extends from the NW to NE Pacific. We found that strong positive correlation regions are not co-located with maximum O_3 and CO concentrations in all simulations. Instead, they are located between most polluted and clean areas, reflecting the intrusion of high O_3 (and CO) air from mid-latitudes and low O_3 (and CO) air from the tropics. Fishman and Seiler (1983) and Mauzerall et al. (2000) previously suggested that strong

1   positive O_3-CO correlations in low CO regions may be caused by the depletion of both O_3 and CO

2   in tropical air.

3   All simulations show positive O_3-CO correlations in the SH marine regions, but

4   GMI/MERRA simulates much stronger negative correlations over the equatorial Atlantic. The

5   latter reflects the stronger convection in the LT/MT in MERRA, which will be discussed below.

6   Positive O_3-CO correlations were previously observed over the tropical South Atlantic during the

7   TRACE-A aircraft mission (September–October, 1992) (e.g., Collins et al., 1996). Collins et al.

8   concluded that the O_3-CO correlations over the tropical South Atlantic are more affected by in situ

9   photochemical production from aged biomass burning plumes (positive O_3-CO correlation) than

10   transport from the stratosphere (negative O_3-CO and O_3 - dew point correlations).

11   Strong positive O_3-CO correlations are present in all simulations at 618 hPa over western

12   and central Indonesia (Figure 12), reflecting convective transport of biomass burning CO (Figure

13   8) and photochemical production of O_3 from its precursors. The dO_3/dCO enhancement ratios over

14   Indonesia are not as large as those over the NH mid-latitude continental outflow regions due to the

15   fact that biomass burning emits NO_x less efficiently than fossil fuel does.

16   Positive O_3-CO correlations over the westerly African biomass burning outflow region

17   (southern Indian Ocean, ~ 45ºS) are seen in all simulations (Figure 12). The positive O_3-CO

18   correlations over both the NH mid-latitude continental outflow regions and the westerly African

19   biomass burning outflow regions mainly reflect O_3 and CO signatures from different sources: 1)

20   anthropogenic emissions of CO and other O_3 precursors in the former and biomass burning

21   emissions in the latter (Figure 8), and 2) significant influences from the stratosphere and

22   subsidence from UT/LS (Figure 9, middle and right columns, respectively). In the case of 1), the

1   dO$_3$/dCO slopes in the westerly African biomass burning outflow are smaller than those in the NH

2   mid-latitude continental outflow, again reflecting the lower efficiency of biomass burning NO$_x$

3   emissions than that of fossil fuel NO$_x$ emissions. In the case of 2), mixing of stratospheric air (high

4   O$_3$) with polluted air masses (high CO) has previously been found associated with positive O$_3$-CO

5   correlations downwind from outflow regions (Cooper et al., 2002; Kim et al., 2013).

6   Strong negative O$_3$-CO correlations are seen in all simulations over the northern tropical

7   eastern Pacific, Caribbean, northern tropical Atlantic, and equatorial Africa. These negative

8   correlations are primarily a result of convective transport of low-O$_3$ air masses impacted by

9   biogenic emissions. As will be discussed in Section 6, significant decreases in O$_3$ and increases in

10   CO occur near the above regions due to atmospheric oxidation of biogenic VOCs (e.g., isoprene)

11   over tropical America and Africa. In addition, our results show weak positive (in GMI/fvGCM

12   and GMI/GEOS4) or strong negative (in GMI/MERRA) O$_3$-CO correlations over much of the

13   southern tropics and subtropics, especially near the biomass burning outflow regions. Negative

14   O$_3$-CO correlations in the southern tropics during July-August were previously reported by

15   Fishman and Seiler (1983). Based on aircraft measurements, they concluded that O$_3$ destruction in

16   the southern tropical LT, where the major CO sources (biomass burning emissions) are located,

17   may lead to strong negative correlations (see their Figure 3).

18   All GMI simulations show strong negative O$_3$-CO correlations over the Asian continent

19   including the Middle East (Figure 12). Over Southwest China (e.g., Sichuan Basin), monsoonal

20   convective lifting of air masses with high-CO and low-O$_3$ leads to negative O$_3$-CO correlations.

21   For most of other regions, high O$_3$ and low CO associated with stratospherically influenced air

22   (Figure 9, middle column) result in negative O$_3$-CO correlations with large (negative) dO$_3$/dCO

23   ratios. As will be discussed in Section 6, lightning NO$_x$ emissions also contribute to these negative

correlations over the Asian continent. Our simulations over the Tibetan Plateau are consistent with the study of Wang et al., (2006), who inferred negative O_3-CO correlations from in situ measurements at Mount Waliguan located at the northeastern edge of the Tibetan Plateau during summer due to downward transport from the UT/LS.

While the O_3-CO correlations in the three simulations show similarities, they also show differences. The global O_3-CO correlation patterns in GMI/fvGCM and GMI/GEOS4 are more similar, presumably because fvGCM is the GCM in the GEOS4 assimilation and they use the same convection scheme. Even so, significantly different O_3-CO correlation coefficients between GMI/fvGCM and GMI/GEOS4 are seen in northern Africa, where the former simulates strong negative but the latter shows weak positive correlations. As indicated by radionuclide tracers (^{210}Pb and ^{7}Be), fvGCM has relatively stronger large-scale subsidence over northern Africa at 618 hPa than GEOS4, resulting in strong correlations with a large negative slope. In addition, the O_3-CO correlations in GMI/MERRA are strongly negative over northern South America, tropical western South Atlantic Ocean, Indian Ocean, and tropical western Pacific Ocean. By contrast, the correlations in these regions in GMI/fvGCM and GMI/GEOS4 are either weak or positive. The convection in fvGCM is much weaker than in GEOS4 or MERRA except at SH mid-latitudes and over Tibetan Plateau (not shown). MERRA has the strongest convection in Central America, tropical western Pacific Ocean, tropical eastern Pacific Ocean, tropical western Atlantic Ocean, tropical eastern Indian Ocean, and Bay of Bengal. These differences of convective mass fluxes result in broader regions with negative O_3-CO correlations in the tropics in GMI/MERRA than those in GMI/fvGCM and GMI/GEOS4. Kim et al. (2013) also simulated different O_3-CO correlations in some tropical regions with GEOS-Chem driven by GEOS4 and GEOS5 meteorological data sets because of the model transport error associated with deep convection.

5.2. Evaluation of GMI O$_3$-CO Correlations with TES Observations

Figures 13 and 14 show the O$_3$-CO correlation coefficients (R) and linear regression slopes (dO$_3$/dCO), respectively, at 618 hPa as determined by TES observations for July - August 2005, and corresponding GMI CTM results with 3-hourly output sampled along the TES orbit tracks. Values are calculated in 10°x10° grid cells. The regions of > 60°S and > 60°N are excluded in this study because O$_3$ and CO concentrations over these regions are low (Figure 8) and absolute co-variances of O$_3$ and CO over these regions are also low (not shown). Therefore, as suggested by Voulgarakis et al. (2011), discrepancies in these regions are not scientifically important in terms of the O$_3$-CO correlation. Since only two months of TES O$_3$ and CO observations were used, the correlation patterns are somewhat patchy and correlations are weak (|R| < 0.2) over more than half of the globe. Using TES data for July – August over 5 years improves the consistency of the correlation patterns (Figure 15), as discussed later. TES-observed O$_3$ and CO concentrations show highest correlations (R up to 0.6) with large slopes over the western Pacific, and relatively high correlations (R = 0.2-0.4) with relatively large slopes over North America, the Middle East, northern South America, central and southern Africa, as well as continental outflow regions, e.g., northwestern Pacific Ocean, western Indian Ocean, subtropical South Atlantic Ocean, tropical eastern Pacific, and northwestern Atlantic (Figures 13 and 14). Negative correlations were observed over the Tibetan Plateau (R < -0.6), northern Africa, and SH mid-latitudes (R < -0.4) (Figure 13). Global TES O$_3$-CO correlation patterns and magnitudes are similar to those reported by Zhang et al. (2006) and Voulgarakis et al. (2011). The slope patterns (Figure 14) follow the correlation ones (Figure 13), suggesting that the slopes of the regression lines are useful indicators of the correlation strength.

The GMI simulated O_3-CO correlation coefficients and linear regression slopes (dO_3/dCO) calculated from each of the three model outputs sampled along the TES orbit tracks show similar global patterns but overall weaker correlations (Figure 13) and smaller slopes (Figure 14) than non-sampled raw model results (Figure 12) due to spatiotemporal sampling and application of TES averaging kernels. All simulations capture the TES-observed positive O_3-CO correlations in various regions. On the other hand, all simulations indicate strong negative correlations over the Tibetan Plateau and tropical convective regions where TES misses such correlations or only shows much weaker negative correlations in much narrower areas.

To get a more statistically robust view of TES O_3-CO correlations, we conduct a similar analysis using multi-year observations. Figure 15 shows the O_3-CO correlation coefficients (R) and linear regression slopes (dO_3/dCO) at 618 hPa as determined by TES O_3 and CO retrievals for July - August over 5 years (2005 – 2009). Values are calculated in 4°x5° grid cells. The global distributions provide more details and are consistent with the coarse patterns for July – August 2005 shown in Figures 13 and 14. The negative correlations over the Tibetan Plateau and northern Africa are more apparent than those using the TES data only for July – August 2005 (Figure 13). Overall our results of multi-year (2005 – 2009) O_3-CO correlation coefficients at 618 hPa for July – August are similar to those inferred from the mean mid-tropospheric (400 – 800 hPa) TES O_3 and CO concentrations averaged over July – August 2005 – 2008 (Voulgarakis et al., 2011).

6. Sensitivity of O_3-CO Correlations to Emissions

In order to understand how O_3-CO correlation patterns are driven by emissions, we examine the sensitivity of O_3-CO correlations to emission types in the GMI model driven by the

MERRA meteorological fields, which represent the state-of-the-art of GEOS-DAS at the time of this study. Figures 16 - 19 show the mean changes in O_3 and CO concentrations (ppbv) and their correlation coefficients, as well as the areas where correlation signs change relative to the standard simulation at 618 hPa when each emission type (fossil fuel, biomass burning, biogenic, and lightning NO_x emissions) is excluded in the model for July – August 2005. Figure 20 shows the O_3-CO correlation coefficients (R) at 618 hPa in the standard simulation and when each emission type is excluded. Results are calculated using 3-hourly model output. These figures provide the context for discussions in this section.

Fossil fuel emissions substantially increase O_3 (by ~5-20 ppbv) and CO (by ~10-30 ppbv) in the NH, notably over the Asian and North American continental outflow regions (Figure 16ab). Fossil fuel emissions lead to strengthened O_3-CO correlations with correlation signs changing from negative to positive over the Asian and North American outflow regions (Figures 16cd and 20b). Such effects are also seen over Europe, the Arabian Sea, the northern Bay of Bengal, and the northeastern Pacific (Figure 16cd). Fossil fuel emissions result in stronger negative O_3-CO correlations over part of the Asian continent (Figure 16c). This is especially true over the Tibetan Plateau where low-level convergence transports air masses with low-O_3 and high-CO to the middle troposphere.

Biomass burning emissions increase O_3 (by ~2-10 ppbv) and CO (by > 25ppbv) in the easterly outflow in the tropical South America and Central Africa, in the westerly outflow in the southern subtropics, and over Indonesia (Figure 17ab). They are responsible for the positive correlations in the SH mid- and high- latitudes (Figures 17cd and 19c). Without biomass burning emissions, O_3-CO correlations over the westerly outflow in the southern subtropics and most of the SH mid- and high- latitudes would be negative or very weak (Figures 17c and 20c). By contrast,

biomass burning emissions degrade an already strong correlation from fossil fuel emissions in the NH (e.g., over part of the tropical western Pacific, Bay of Bengal, NH subtropical Atlantic, and especially NH high latitudes, Figure 17d). In the tropics, biomass burning emissions strengthen the positive correlations in Indonesia and weaken the negative correlations over the tropical South American outflow region. In the two models of Voulgarakis et al. (2011), biomass burning emissions have the largest impact on the O_3-CO correlations in the tropics, especially downwind of Central Africa and South America where biomass burning emissions changed the correlation sign from negative to positive. Our results show no apparent changes in the O_3-CO correlation signs (negative) in these downwind regions. This may reflect the differences in biomass burning emissions and/or chemical mechanisms used in the two studies.

Biogenic emissions increase O_3 concentrations at 618 hPa by ~ 2-6 ppbv in the NH subtropics and mid-latitudes, but decrease O_3 concentrations by up to ~10 ppbv in tropical South America, tropical Africa, and Indonesia (Figure 18a). The latter mainly reflects the fact that O_3 is consumed during the atmospheric oxidation process of isoprene under low NO_X conditions (Fan and Zhang, 2004; Seinfeld and Pandis, 1998). Biogenic emissions have large positive impacts on CO concentrations in the easterly and westerly outflow regions of South America and Africa, in the North American outflow, over Southwest China and Indonesia, as well as in the SH background (Figure 18b). The O_3-CO correlations in the model show smaller sensitivity to biogenic emissions relative to other emission types (Figures 18c and 20d). Nevertheless, biogenic emissions lead to strong negative O_3-CO correlations over the tropical eastern Pacific Ocean due to reduced O_3 and enhanced CO concentrations associated with these emissions (Figures 18cd and 20d). Such effects are also seen over central Africa, easterly South American outflow, westerly South American outflow, Indonesia, and subtropical western Pacific.

1   Lightning NO_X emissions increase O_3 concentrations at 618 hPa by up to ~15-25 ppbv at

2   NH subtropics and mid-latitudes, and by up to ~15-30 ppbv at SH tropics and subtropics (Figure

3   19a). Such increases are relatively larger in those regions with subsiding air from the UT (cf.,

4   Figure 9, right bottom panel), where the largest effect of lightning NO_X emissions occurs. The

5   resulting increase in OH concentrations leads to a general decrease in CO concentrations with

6   maximum effects in the tropics and SH subtropics (Figure 19ab). Consequently, lightning NO_X

7   emissions weaken both the positive O_3-CO correlations at mid- and high- latitudes and the negative

8   correlations in the tropics (Figures 19cd and 20e). They alter the correlation signs from positive to

9   negative in various areas where the correlations are generally weak (Figure 19d). Our results are

10   in contrast with those of Voulgarakis et al. (2011) who showed that lightning NO_X emissions

11   appeared to increase the O_3-CO correlations (400-800 hPa) in various regions (e.g., tropical eastern

12   Pacific, NH continental outflow regions). These may partly reflect the differences in the altitude

13   and strength of lightning NO_x emissions.

15   **7. Summary and Conclusions**

16   We have examined the capability of the Global Modeling Initiative (GMI) chemistry and

17   transport model (CTM) to reproduce the global mid-tropospheric O_3-CO correlations from the TES

18   instrument onboard the NASA Aura satellite during boreal summer (July – August). The model

19   was driven by three meteorological data sets (fvGCM for 1995, GEOS4 for 2005, MERRA for

20   2005), allowing us to examine the sensitivity of model O_3-CO correlations to input meteorological

21   data. To understand how various emissions drive global O_3-CO correlation patterns, we also

1   investigated the sensitivity of GMI/MERRA model-calculated O_3 and CO concentrations and their

2   correlations to emission types.

3   We evaluated GMI-simulated tropospheric O_3 vertical profiles and tropospheric O_3

4   columns (TOCs) with those from ozonesonde and satellite observations, respectively. To aid in

5   the evaluation, model simulations of radionuclide tracers (^{222}Rn, ^{210}Pb, and ^{7}Be) were used to

6   illustrate the differences in convection, stratospheric influence, and large-scale subsidence among

7   three meteorological data sets. Among the three GMI simulations, GMI/GEOS4-simulated O_3

8   concentrations are in best agreement with the observations. GMI/MERRA underestimates O_3 in

9   the NH high-latitude UT due to weak STE, and overestimates O_3 in the SH subtropics. The latter

10   is due to a combination of excessive influences from lightning NO_x emissions and STE (or

11   subsidence), as well as the shallower convection resulting in less low-O_3 air lifted from the LT to

12   MT/UT. The latitudinal distribution of model biases in TOCs relative to satellite observations is

13   consistent with the results from model evaluations with ozonesonde O_3 profiles.

14   We evaluated GMI simulated O_3 and CO concentrations with TES observations at 618 hPa

15   where TES has most sensitivity. TES observed O_3 enhancements over the NH mid-latitudes

16   (including continental outflow regions), the Middle East, and the subtropical southern Africa and

17   Atlantic. All simulations well capture the global spatial distribution of O_3 at 618 hPa, but appear

18   to underestimate TES O_3 observations over southern Africa and its outflow region. GMI/fvGCM

19   simulates the highest O_3 concentrations at NH mid-/high-latitudes, especially the Asian continent

20   due to strong STE whereas it simulates the lowest O_3 concentrations in the southern tropics and

21   subtropics due to weak STE and low lightning NO_X emissions. GMI/MERRA simulates the highest

22   O_3 concentrations in the southern subtropics, especially southern Africa due to high lightning NO_x

23   emissions and, to a lesser extent, strong convection. GMI/fvGCM underestimates the O_3 minimum

1   in the tropical western Pacific and eastern Indian Ocean. Considering the positive bias in TES O_3

2   at NH mid-latitudes, GMI/fvGCM appears to overestimate O_3 over the East Asian outflow region

3   due to too fast STE whereas GMI/GEOS4 and GMI/MERRA simulate O_3 enhancements

4   reasonably well in East Asia and its downwind regions. All three simulations significantly

5   underestimate TES-observed CO enhancements at NH mid-latitudes, but simulate better CO

6   enhancements over the tropical biomass burning regions.

7   The three GMI simulations all show strong positive O_3-CO correlations at 618 hPa over

8   the NH mid-latitude continental outflow regions and the SH biomass burning outflow regions, as

9   shown by TES observations. Generally, positive O_3-CO correlations are simulated downwind of

10   polluted regions due to photochemical production of O_3 from its precursors. However, owing to

11   significant influences from the stratosphere and subsidence from UT/LS over these regions, mixing

12   of stratospheric air with polluted (anthropogenic or biomass burning) air masses is associated with

13   strong positive O_3-CO correlations with large dO_3/dCO enhancement ratios. Strong positive O_3-

14   CO correlations are also simulated over the Indonesian biomass burning region where deep

15   convection occurs, but the dO_3/dCO enhancement ratios are smaller than those in the NH mid-

16   latitude continental outflow regions. The latter reflects the lower efficiency of NO_X emissions from

17   biomass burning. Strong negative O_3-CO correlations over northern and central Africa, tropical

18   Atlantic, and tropical eastern and western Pacific in all simulations result from convective

19   transport of biomass burning air masses with low-O_3, and consumption of O_3 along with

20   production of CO due to oxidation of biogenic hydrocarbons (e.g., isoprene under low NO_x

21   conditions). The simulated negative O_3-CO correlations over the Asian continent, including the

22   Middle East, are partly attributed to stratospheric influence and/or subsidence from UT/LS. High-

23   O_3 and low-CO associated with stratospherically influenced air lead to strong negative correlations

with large dO_3/dCO ratios. On the other hand, over Southwest China, monsoonal convective lifting of air masses with high-CO and low-O_3 results in negative O_3-CO correlations. By contrast, TES O_3 and CO concentrations at 618 hPa either miss such negative correlations (i.e., tropical convective regions) or only show weak negative correlations over much narrower areas (i.e., the Tibetan Plateau and northern Africa).

TES-observed O_3 and CO concentrations at 618 hPa show highest positive correlations with large regression slopes over the western Pacific, and relatively high correlations over North America, the Middle East, northern South America, central and southern Africa, and continental outflow regions. Negative correlations are observed in parts of the Asian continent (Tibetan Plateau), northern Africa, and SH mid-latitudes. All model output sampled along the TES orbit track capture the observed positive O_3-CO correlations over the NH mid-latitude continental outflow regions, southern Africa, western Indian Ocean, subtropical South Atlantic, northern South America, and tropical eastern Pacific. While all simulations show strong negative correlations over the Tibetan Plateau, northern Africa, northern subtropical eastern Pacific, and Caribbean, TES O_3 and CO concentrations at 618 hPa only show weak negative correlations over much narrower areas (i.e., the Tibetan Plateau and northern Africa).

We performed sensitivity simulations with GMI/MERRA to investigate the effect of individual emission types on model-calculated O_3-CO correlations at 618 hPa. Results show that fossil fuel emissions increase global O_3 and CO concentrations and are responsible for the strong positive correlations over the NH continental outflow regions. Both biomass burning and biogenic emissions significantly increase global CO concentrations. Biomass burning emissions increase O_3 concentrations in the easterly outflow in the tropical South America and Central Africa, in the westerly outflow in the southern subtropics, and over Indonesia. Biogenic emissions increase O_3

concentrations in the NH subtropics and mid-latitudes, but decrease O_3 concentrations in tropical South America, tropical Africa, and Indonesia. The decreases mainly reflect the fact that O_3 is consumed during the atmospheric oxidation process of isoprene under low NO_x conditions. Biomass burning emissions are responsible for the positive correlations in the SH mid- and high-latitudes and negative correlations over part of the tropical western Pacific, Bay of Bengal, NH subtropical Atlantic, and NH high latitudes. Biogenic emissions have relatively smaller impact on the correlations than other emissions do, but are largely responsible for the negative O_3-CO correlations over the tropical eastern Pacific. Lightning NO_x emissions lead to large increases in O_3 concentrations at NH subtropics and mid-latitudes, and at SH tropics and subtropics, especially in the regions of subsidence. We find that lightning NO_x emissions weaken both positive O_3-CO correlations at mid- and high-latitudes and negative correlations in the tropics, and change weak positive correlations to negative in various areas. This result contrasts with that of previous studies.

This study demonstrates the utility of O_3-CO correlations to constrain the sources of tropospheric O_3 in global 3-D models. Our model simulations driven by three input meteorological data sets show significantly different global and regional distributions of O_3 and CO concentrations during boreal summer. For instance, GMI/fvGCM simulations show higher O_3 concentrations in the NH and lower CO concentrations than other simulations. Despite such differences, all simulations show similar patterns of O_3-CO correlations on a global scale. The regional features of the correlations, however, are often different due to the discrepancies in various meteorological processes (e.g., convection, STE, subsidence). In particular, GMI/MERRA simulates broader areas of strong negative O_3-CO correlations at 618 hPa in the tropics than GMI/fvGCM and GMI/GEOS4 do due to stronger tropical convection in the LT/MT. In this sense, O_3-CO correlations can be used to constrain better the sources of regional tropospheric O_3 in global models,

especially for convective regions than O$_3$ and CO observations individually. Future work, where additional meteorological archives (e.g., GFDL AM3, ECMWF ERA-Interim) may also be incorporated, should examine the driving factors for O$_3$-CO correlations in other seasons.

Data availability

A description of the model output and observational data used in this paper can be found in Sect. 2 and they are available upon request by contacting Hongyu Liu (hongyu.liu-1@nasa.gov).

Acknowledgements. This work was supported by the NASA Modeling, Analysis, and Prediction (MAP) program and NASA Atmospheric Composition Modeling and Analysis Program (ACMAP). NASA Center for Computational Sciences (NCCS) provided supercomputing resources. TES data products are distributed by NASA Langley Atmospheric Science Data Center.

References

Allen, D., Pickering, K., Duncan, B., and Damon, M.: Impact of lightning NO emissions on North American photochemistry as determined using the Global Modeling Initiative (GMI) model, *J. Geophys. Res.*, *115*, D22301, doi:10.1029/2010JD014062, 2010.

Anderson, B. E., Gregory, G. L., Barrick, J. D. W., Collins, J. E. Jr., Sachse, G. W., Bagwell, D., Shipham, M. C., Bradshaw, J. D., and Sandholm, S. T.: The impact of U.S. continental outflow on ozone and aerosol distributions over the western Atlantic, *J. Geophys. Res.*, *98*(D12), 23,477–23,489, doi:10.1029/93JD01208, 1993.

Beer, R., Glavich, T. A., and Rider, D. M.: Tropospheric emission spectrometer for the Earth Observing System's Aura Satellite, *Appl. Optics*, *40*, 2356–2367, 2001.

Beer, R.: TES on the Aura mission: Scientific objectives, measurements, and analysis overview, *IEEE T. Geosci. Remote*, *44*, 1102–1105, doi:10.1109/tgrs.2005.863716, 2006.

Bowman, K. W., Steck, T., Worden, H. M., Worden, J., Clough, S., and Rodgers, C.: Capturing time and vertical variability of tropospheric ozone: A study using TES nadir retrievals, *J. Geophys. Res.*,*107*(D23), 4723, doi:10.1029/2002JD002150, 2002.

Bowman, K. W., et al.: Tropospheric emission spectrometer: Retrieval method and error analysis, *IEEE T. Geosci. Remote*, *44*, 1297–1307, doi:10.1109/tgrs.2006871234, 2006.

Benkovitz, C. M., Scholtz, M. T., Pacyna, J., Tarrasón, L., Dignon, J., Voldner, E. C., Spiro, P. A., Logan, J. A., and Graedel, T. E.: Global gridded inventories of anthropogenic emissions of sulfur and nitrogen, *J. Geophys. Res.*, *101*(D22), 29239–29253, doi:10.1029/96JD00126, 1996.

Bey, I., Jacob, D.J., Yantosca, R.M., Logan, J.A., Field, B., Fiore, A.M., Li, Q., Liu, H., Mickley, L.J., and Schultz, M.: Global modeling of tropospheric chemistry with assimilated meteorology: Model description and evaluation, *J. Geophys. Res., 106*, 23,073-23,096, 2001.

Bloom, S., Silva, A. da, Dee, D., Bosilovich, M., Chern, J.-D., Pawson, S., Schubert, S., Sienkiewicz, M., Stajner, I., Tan, W.-W., and Wu, M.-L.: Documentation and Validation of the Goddard Earth Observing System (GEOS) Data Assimilation System - Version 4. *Technical Report Series on Global Modeling and Data Assimilation* (Editor Max J. Suarez), NASA/TM-2005-104606, Vol. 26, NASA Goddard Space Flight Center, Greenbelt, Maryland, April 2005, 2005.

Chin, M., Jacob, D. J., Munger, J. W., Parrish, D. D., and Doddridge, B. G.: Relationship of ozone and carbon monoxide over North America, *J. Geophys. Res.*, *99*(D7), 14,565–14,573, doi:10.1029/94JD00907, 1994.

Chandra, S., Ziemke, J. R., Duncan, B. N., Diehl, T. L., Livesey, N. J., and Froidevaux, L.: Effects of the 2006 El Niño on tropospheric ozone and carbon monoxide: implications for dynamics and biomass burning, *Atmos. Chem. Phys.*, *9*, 4239-4249, doi:10.5194/acp-9-4239-2009, 2009.

Collins Jr., J. E., Anderson, B. E., Sachse, G. W., J. Barrick, D. W., Wade, L. O., Burney, L. G., and Hill , G. F.: Atmospheric fine structure during GTE TRACE A: Relationships among ozone, carbon monoxide, and water vapor, *J. Geophys. Res.*, *101*(D19), 24307–24316, doi:10.1029/96JD02180, 1996.

Considine, D. B., Bergmann, D. J., and Liu, H.: Sensitivity of Global Modeling Initiative chemistry and transport model simulations of radon-222 and lead-210 to input meteorological data, *Atmos. Chem. Phys.*, *5*, 3389-3406, doi:10.5194/acp-5-3389-2005, 2005.

Considine, D. B., Logan, J. A., and Olsen, M. A.: Evaluation of near-tropopause ozone distributions in the Global Modeling Initiative combined stratosphere/troposphere model with ozonesonde data, *Atmos. Chem. Phys.*, *8*, 2365-2385, doi:10.5194/acp-8-2365-2008, 2008.

Cooper, O. R., Moody, J. L., Parrish, D. D., Trainer, M., Holloway, J. S., Hübler, G., Fehsenfeld, F. C., and Stohl, A.: Trace gas composition of midlatitude cyclones over the western North Atlantic Ocean: A seasonal comparison of O_3 and CO, *J. Geophys. Res.*, *107*(D7), doi:10.1029/2001JD000902, 2002.

Dibb, J. E., Meeker, L. D., Finkel, R. C., Southon, J. R., Caffee, M. W., and Barrie, L. A.: Estimation of stratospheric input to the Arctic troposphere: ^{7}Be and ^{10}Be in aerosols at Alert, Canada, *J. Geophys. Res.*, *99*, 12,855-12,864, 1994.

Douglass, A.R., Prather, M.J., Hall, T.M., Strahan, S.E., Rasch, P.J., Sparling, L.C., Coy, L., and Rodriguez, J.M.: Choosing meteorological input for the global modeling initiative assessment of high-speed aircraft, *J. Geophys. Res., 104*(D22), 27,545-27,564, 1999.

Douglass, A. R., Stolarski, R. S., Strahan, S. E., and Connell, P. S.: Radicals and reservoirs in the GMI chemistry and transport model: Comparison to measurements, *J. Geophys. Res.*, *109*, D16302, doi:10.1029/2004JD004632, 2004.

Duncan, B. N., Martin, R., Staudt, A., Yevich, R., and Logan, J.: Interannual and Seasonal Variability of Biomass Burning Emissions Constrained by Satellite Observations, *J. Geophys. Res.*, *108*(D2), 4100, doi:10.1029/2002JD002378, 2003.

Duncan, B. N., Strahan, S. E., Yoshida, Y., Steenrod, S. D., and Livesey, N.: Model study of the cross-tropopause transport of biomass burning pollution, *Atmos. Chem. Phys.*, *7*, 3713-3736, doi:10.5194/acp-7-3713-2007, 2007a.

Duncan, B. N., Logan, J. A., Bey, I., Megretskaia, I. A., Yantosca, R. M., Novelli, P. C., Jones, N. B., and Rinsland, C. P.: Global budget of CO, 1988–1997: Source estimates and validation with a global model, *J. Geophys. Res.*, *112*, D22301, doi:10.1029/2007JD008459, 2007b.

Duncan, B. N., West, J. J., Yoshida, Y., Fiore, A. M., and Ziemke, J. R.: The influence of European pollution on ozone in the Near East and northern Africa, *Atmos. Chem. Phys.*, *8*, 2267-2283, doi:10.5194/acp-8-2267-2008, 2008.

Fan, J. and Zhang, R.: Atmospheric oxidation mechanism of Isoprene, *Environ. Chem.*, 1, 140-149, doi: 10.1071/EV04045, 2004.

Fehsenfeld, F. C., Daum, P., Leaitch, W. R., Trainer, M., Parrish, D. D., and Hübler, G.: Transport and processing of O_3 and O_3 precursors over the North Atlantic: An overview of the 1993 North Atlantic Regional Experiment (NARE) summer intensive, *J. Geophys. Res.*, 101(D22), 28,877–28,891, doi:10.1029/96JD01113, 1996.

Fishman, J., and Seiler, W.: Correlative nature of ozone and carbon monoxide in the troposphere: Implications for the tropospheric ozone budget, *J. Geophys. Res.*, *88*, 3662–3670, 1983.

Fishman, J., Wozniak, A. E., and Creilson, J. K.: Global distribution of tropospheric ozone from satellite measurements using the empirically corrected tropospheric ozone residual technique: Identification of the regional aspects of air pollution, *Atmos. Chem. Phys., 3,* 893-907, 2003.

Guenther, A., Karl, T., Harley, P., Wiedinmyer, C., Palmer, P.I., and Geron, C.: Estimates of global terrestrial isoprene emissions using MEGAN (Model of Emissions of Gases and Aerosols from Nature), *Atmos. Chem. Phys.*, *6*, 3181-3210, 2006.

Hack, J. J.: Parameterization of moist convection in the National Center for Atmospheric Research Community Climate Model (CCM2), J. Geophys. Res., 99, 5551–5568, 1994.

Honrath, R. E., Owen, R. C., Val Martín, M., Reid, J. S., Lapina, K., Fialho, P., Dziobak, M. P., Kleissl, J., and Westphal, D. L.: Regional and hemispheric impacts of anthropogenic and biomass burning emissions on summertime CO and O_3 in the North Atlantic lower free troposphere, *J. Geophys. Res.*, *109*, D24310, doi:10.1029/2004JD005147, 2004.

Hsu, J., Prather, M. J., Wild, O., Sundet, J. K., Isaksen, I. S. A., Browell, E. V., Avery, M. A., and Sachse, G. W.: Are the TRACE-P measurements representative of the western Pacific during March 2001?, *J. Geophys. Res.*, *109*(D2), D02314, doi:10.1029/2003JD004002, 2004.

Jacob D. J., and Wofsy, S. C.: Budgets of Reactive Nitrogen, Hydrocarbons, and Ozone Over the Amazon Forest During the Wet Season, *J. Geophys. Res.*, *95*, 16,737-16,754, 1990.

Jacob, D. J., et al.: Evaluation and inter-comparison of global atmospheric transport models using 2•Rn and other short-lived tracers, *J. Geophys. Res.*, *102*, 5953-5970, 1997.

Jaffe, D. A., Honrath, R. E., Zhang, L., Akimoto, H., Shimizu, A., Mukai, H., Murano, K., Hatakeyama, S., and Merrill, J.: Measurements of NO, NO_y, CO and O_3 and estimation of the ozone production rate at Oki Island, Japan, during PEM-West, *J. Geophys. Res.*, *101*(D1), 2037–2048, doi:10.1029/95JD01699, 1996.

Kim, P. S., Jacob, D. J., Liu, X., Warner, J. X., Yang, K., Chance, K., Thouret, V., and Nedelec, P.: Global ozone–CO correlations from OMI and AIRS: constraints on tropospheric ozone sources, *Atmos. Chem. Phys., 13,* 9321-9335, doi:10.5194/acp-13-9321-2013, 2013.

Kinnison, D. E., et al.: The Global Modeling Initiative assessment model: Application to high-speed civil transport perturbation*, J. Geophys. Res., 106(*D2*), 1693–1711, doi:*10.1029/2000JD900406, 2001.

Koch, D. M., and Mann, M. E.: Spatial and temporal variability of ^{7}Be surface concentration, *Tellus*, *Ser. B*, *48*, 387-396, 1996.

Li, Q., Jacob, D. J., Bey, I., Palmer, P. I., Duncan, B. N., Field, B. D., Martin, R. V., Fiore, A. M., Yantosca, R. M., Parrish, D. D., Simmonds, P. G., and Oltmans, S. J.: Transatlantic transport of pollution and its effects on surface ozone in Europe and North America, *J. Geophys. Res.*, *107*(D13), doi:10.1029/2001JD001422, 2002.

Lin, S.-J., and Rood, R. B.: Multidimensional flux-form semi-Lagrangian transport schemes, *Mon. Weather Rev.*, *124*, 2046–2070, 1996.

Liu, H., Jacob, D. J., Bey, I., and Yantosca, R. M.: Constraints from ^{210}Pb and ^{7}Be on wet deposition and transport in a global three-dimensional chemical tracer model driven by assimilated meteorological fields, *J. Geophys. Res., 106(*D11*),* 12109–12128, *doi:*10.1029/2000JD900839, 2001.

Liu, H., Considine, D. B., Horowitz, L. W., Crawford, J. H., Rodriguez, J. M., Strahan, S. E., Damon, M. R., Steenrod, S. D., Xu, X., Kouatchou, J., Carouge, C., and Yantosca, R. M.: Using beryllium-7 to assess cross-tropopause transport in global models, Atmos. Chem. Phys., 16, 4641-4659, doi:10.5194/acp-16-4641-2016, 2016.

Liu, J., Logan, J. A., Jones, D. B. A., Livesey, N. J., Megretskaia, I., Carouge, C., and Nedelec, P.: Analysis of CO in the tropical troposphere using Aura satellite data and the GEOS-Chem model: insights into transport characteristics of the GEOS meteorological products, *Atmos. Chem. Phys.*, *10*, 12207-12232, doi:10.5194/acp-10-12207-2010, 2010.

Logan, J. A. (1999), An analysis of ozonesonde data for the troposphere: Recommendations for testing 3-D models and development of a gridded climatology for tropospheric ozone, *J. Geophys. Res.*, *104*, 16 115–16 149.

Lopez, J. P., Luo, M., Christensen, L. E., Loewenstein, M., Jost, H., Webster, C. R., and Osterman, G.: TES carbon monoxide validation during two AVE campaigns using the Argus and ALIAS instruments on NASA's WB-57F, *J. Geophys. Res.*, *113*, D16S47, doi:10.1029/2007JD008811, 2008.

Luo, M., et al.: TES carbon monoxide validation with DACOM aircraft measurements during INTEX-B 2006, *J. Geophys. Res.*, *112*, D24S48, doi:10.1029/2007JD008803, 2007a.

Luo, M., et al.: Comparison of carbon monoxide measurements by TES and MOPITT: Influence of a priori data and instrument characteristics on nadir atmospheric species retrievals, J. Geophys. Res., 112, D09303, doi:10.1029/2006JD007663, 2007b.

Mao, H., and Talbot, R.: O_3 and CO in New England: Temporal variations and relationships, *J. Geophys. Res.*, *109*, D21304, doi:10.1029/2004JD004913, 2004.

Mari, C., Jacob, D. J., and Bechtold, P.: Transport and scavenging of soluble gases in a deep convective cloud, *J. Geophys. Res.*, *105*, 22,255-22,267, 2000.

Mauzerall, D. L., Narita, D., Akimoto, H., Horowitz, L., Walters, S., Hauglustaine, D. A., and Brasseur, G.: Seasonal characteristics of tropospheric ozone production and mixing ratios over East Asia: A global three-dimensional chemical transport model analysis, *J. Geophys. Res.*, *105*(D14), 17,895–17,910, doi:10.1029/2000JD900087, 2000.

Moorthi S. and Suarez, M. J.: Relazed Arakawa-Shubert. A Parameterization of moist convection for general circulation models, *Mon. Weather Rev., 120*, 978-1002, 1992.

Naja, M., Lal, S., and Chand, D.: Diurnal and seasonal variabilities in surface ozone at a high altitude site Mt Abu (24.6 degrees N, 72.7 degrees E, 1680 m asl) in India, *Atmos. Environ.*, *37*, 4205–4215, doi:10.1016/S1352-2310(03)00565-X, 2003.

Nassar, R., et al.: Validation of Tropospheric Emission Spectrometer (TES) nadir ozone profiles using ozonesonde measurements, *J. Geophys. Res.*, *113*, D15S17, doi:10.1029/2007JD008819, 2008.

Osterman, G. B., Kulawik, S. S., Worden, H., Richards, N. A., Fisher, B. M., Eldering, A., Shephard, M. W., Froidevaux, L., Labow, G., Luo, M., Herman, R. L., Bowman, K. W., and Thompson, A. M.: Validation of Tropospheric Emission Spectrometer (TES) measurements

of the total, stratospheric, and tropospheric column abundance of ozone, J. Geophys. Res., 113, D15S16, doi:10.1029/2007JD008801, 2008.

Parrington, M.*,* Jones, D. B. A.*,* Bowman, K. W.*,* Horowitz, L. W.*,* Thompson, A. M.*,* Tarasick, D. W.*,* and Witte, J. C.: Estimating the summertime tropospheric ozone distribution over North America through assimilation of observations from the Tropospheric Emission Spectrometer*, J. Geophys. Res., 113, D18307, doi:*10.1029/2007JD009341, 2008*.*

Parrish, D. D., Holloway, J. S., Trainer, M., Murphy, P. C., Forbes, G. L., and Fehsenfeld, F. C.: Export of North American Ozone Pollution to the North Atlantic Ocean, *Science*, *259*, 1436–1439, 1993.

Parrish, D. D., Trainer, M., Holloway, J. S., Yee, J. E., Warshawasky, M. S., and Fehsenfeld, F. C.: Relationships between ozone and carbon monoxide at surface sites in the North Atlantic region, *J. Geophys. Res.*, *103*(D11), 13357–13376, 1998.

Real, E., Law, K. S., Schlager, H., Roiger, A., Huntrieser, H., Methven, J., Cain, M., Holloway, J., Neuman, J. A., Ryerson, T., Flocke, F., Gouw, J. de, Atlas, E., Donnelly, S., and Parrish, D.: Lagrangian analysis of low altitude anthropogenic plume processing across the North Atlantic, *Atmos. Chem. Phys.*, *8*, 7737– 7754, doi:10.5194/acp-8-7737-2008, 2008.

Rotman, D. A., et al.: Global Modeling Initiative assessment model: Model description, integration, and testing of the transport shell, *J. Geophys. Res.*, *106*, 1669–1691, 2001.

Schoeberl, M. R., Duncan, B. N., Douglass, A. R., Waters, J., Livesey, N., Read, W., and Filipiak, M.: The carbon monoxide tape recorder, *Geophys. Res. Lett.*, *33*, L12811, doi:10.1029/2006GL026178, 2006.

Seinfeld, J. H., and Pandis, S. N.: Atmospheric Chemistry and Physics, *Wiley*, New York, 1998.

Shim, C., Li, Q., Luo, M., Kulawik, S., Worden, H., Worden, J., Eldering, A., Diskin, G., Sachse, G., Weinheimer, A., Knapp, D., Montzca, D., and Campos, T.: Satellite observations of Mexico City pollution outflow from the Tropospheric Emissions Spectrometer (TES), *Atmos. Environ.*, *43*, 1540–1547, doi:10.1016/j.atmosenv.2008.11.026, 2009.

Shindell, D. T., et al.: Multimodel simulations of carbon monoxide: Comparison with observations and projected near-future changes, J. Geophys. Res., 111, D19306, doi:10.1029/2006JD007100, 2006.

Strahan, S. E., Duncan, B. N., and Hoor, P.: Observationally derived transport diagnostics for the lowermost stratosphere and their application to the GMI chemistry and transport model, *Atmos. Chem. Phys.*, *7*, 2435-2445, doi:10.5194/acp-7-2435-2007, 2007.

Thompson, A. M., Pickering, K. E., McNamara, D. P., Schoeberl, M. R., Hudson, R. D., Kim, J. H., Browell, E. V., Kirchhoff, V. W. J. H., and Nganga, D.: Where did tropospheric ozone over southern Africa and the tropical Atlantic come from in October 1992? Insights from TOMS, GTE TRACE A, and SAFARI 1992, *J. Geophys. Res.*, *101*(D19), 24,251–24,278, doi:10.1029/96JD01463, 1996.

Thompson, A. M., Witte, J. C., McPeters, R. D., et al.: Southern Hemisphere Additional Ozonesondes (SHADOZ) 1998–2000 tropical ozone climatology – 1. Comparison with Total Ozone Mapping Spectrometer (TOMS) and ground-based measurements, *J. Geophys. Res.*, 108(D2), 8238, doi:10.1029/2001JD000967, 2003.

Tsutsumi, Y., and Matsueda, H.: Relationship of ozone and CO at the summit of Mt. Fuji (35.35 degrees N, 138.73 degrees E, 3776 m above sea level) in summer 1997, *Atmos. Environ.*, *34*, 553– 561, 2000.

1   Voulgarakis, A., Telford, P. J., Aghedo, A. M., Braesicke, P., Faluvegi, G., Abraham, N. L.,

2   Bowman, K. W., Pyle, J. A., and Shindell, D. T.: Global multi-year O_3-CO correlation

3   patterns from models and TES satellite observations, *Atmos. Chem. Phys.*, *11*, 5819-5838,

4   doi:10.5194/acp-11-5819-2011, 2011.

5   Wang, T., Wong, H. L. A., Tang, J., Ding, A., Wu, W. S., and Zhang, X. C.: On the origin of

6   surface ozone and reactive nitrogen observed at a remote mountain site in the northeastern

7   Qinghai-Tibetan Plateau, western China, *J. Geophys. Res.*, 111, D08303,

8   doi:10.1029/2005JD006527, 2006.

9   Worden, J., Kulawik, S. S., Shephard, M. W., Clough, S. A., Worden, H., Bowman, K., and

10   Goldman, A.: Predicted errors of tropospheric emission spectrometer nadir retrievals from

11   spectral window selection, *J. Geophys. Res., 109, D09308, doi:*10.1029/2004JD004522,

12   2004.

13   Worden, H. M., et al.: Comparisons of Tropospheric Emission Spectrometer (TES) ozone profiles

14   to ozonesondes: Methods and initial results, *J. Geophys. Res., 112, D03309,*

15   *doi:*10.1029/2006JD007258, 2007.

16   Yevich, R., and Logan, J. A.: An assesment of biofuel use and burning of agricultural waste in the

17   developing world, *Global Biogeochem. Cycles*, *17*, (4), 1095, doi:10.1029/2002GB001952,

18   2003.

19   Zhang, G. J., and McFarlane, N. A.: Sensitivity of climate simulations to the parameterization of

20   cumulus convection in the Canadian Climate Centre general circulation model, *Atmos.*

21   *Ocean.*, *33*, 407– 446, 1995.

22   Zhang, L., Jacob, D. J., Bowman, K. W., Logan, J. A., Turquety, S., Hudman, R. C., Li, Q., Beer,

23   R., Worden, H. M., Rinsland, C. P., Kulawik, S. S., Lampel, M. C., Shephard, M. W., Fisher,

B. M., Eldering, A., and Avery, M. A.: Ozone-CO correlations determined by the TES satellite instrument in continental outflow regions, *Geophys. Res. Lett.*, *33*, L18804, doi:10.1029/2006GL026399, 2006.

Zhang, L., Li, Q. B., Jin, J., Liu, H., Livesey, N., Jiang, J. H., Mao, Y., Chen, D., Luo, M. , and Chen, Y.: Impacts of 2006 Indonesian fires and dynamics on tropical upper tropospheric carbon monoxide and ozone, *Atmos. Chem. Phys.*, *11*, 10929-10946, doi:10.5194/acp-11-10929-2011, 2011 .

Zhang, L., Li, Q. B., Murray, L. T., Luo, M., Liu, H., Jiang, J. H., Mao, Y., Chen, D., Gao, M., and Livesey, N.: A tropospheric ozone maximum over the equatorial Southern Indian Ocean, *Atmos. Chem. Phys., 12,* 4279-4296, doi:10.5194/acp-12-4279-2012, 2012.

Ziemke, J.R., Chandra, S., Duncan, B. N., Froidevaux, L., Bhartia, P. K., Levelt, P. F., and Waters, J. W.: Tropospheric ozone determined from Aura OMI and MLS: Evaluation of measurements and comparison with the Global Modeling Initiative's Chemical Transport Model, *J. Geophys. Res.*, *111*, D19303, doi:10.1029/2006JD007089, 2006.

Table 1. Global lightning NO_X emissions (Tg N/mon) during May – August in GMI CTM driven
by three meteorological data sets (fvGCM, GEOS4, and MERRA)

	May	June	July	August
fvGCM	0.57 (0.03[a])	0.65 (0.02)	0.80 (0.03)	0.78 (0.05)
GEOS4	0.64 (0.05)	0.73 (0.07)	0.82 (0.03)	0.72 (0.05)
MERRA	0.49 (0.07)	0.69 (0.07)	0.81 (0.03)	0.78(0.04)

[a] Values in parenthesis denote lightning NO_x emissions between 10°S and 70°S.

7 **Table 2**. Mean differences (ppbv) between GMI-simulated O_3 and ozonesonde observations at 500 hPa
8 and 200 hPa, respectively.

Ozonesonde Station	GMI/fvGCM - sonde		GMI/GEOS4 - sonde		GMI/MERRA – sonde	
	500 hPa	200 hPa	500 hPa	200 hPa	500 hPa	200 hPa
Resolute (75^0N, 95^0W)	8.53	48.37	1.72	-65.79	-7.33	-85.56
Churchill (59^0N, 147^0W)	10.52	129.41	-0.30	-8.82	-8.98	-38.87
Hohenpeissenberg (48^0N, 11^0E)	9.53	43.85	4.81	33.60	-3.15	2.20
Sapporo (43^0N, 141^0E)	14.07	41.76	5.58	39.03	-2.95	34.90
Wallops Island (38^0N, 76^0W)	9.21	-11.07	13.14	-14.83	6.41	-6.91
Paramaribo (6^0N, 55^0W)	-9.46	-8.11	-10.74	-19.83	-12.84	7.38
Nairobi (1^0S, 37^0E)	-10.94	-15.53	-4.35	-15.91	-1.62	-8.20
Samoa (14^0S, 170^0W)	-5.33	-7.27	-2.45	-4.01	17.22	27.85
Reunion Island (21^0S, 55^0E)	-11.49	-17.30	0.51	-2.50	8.38	16.91
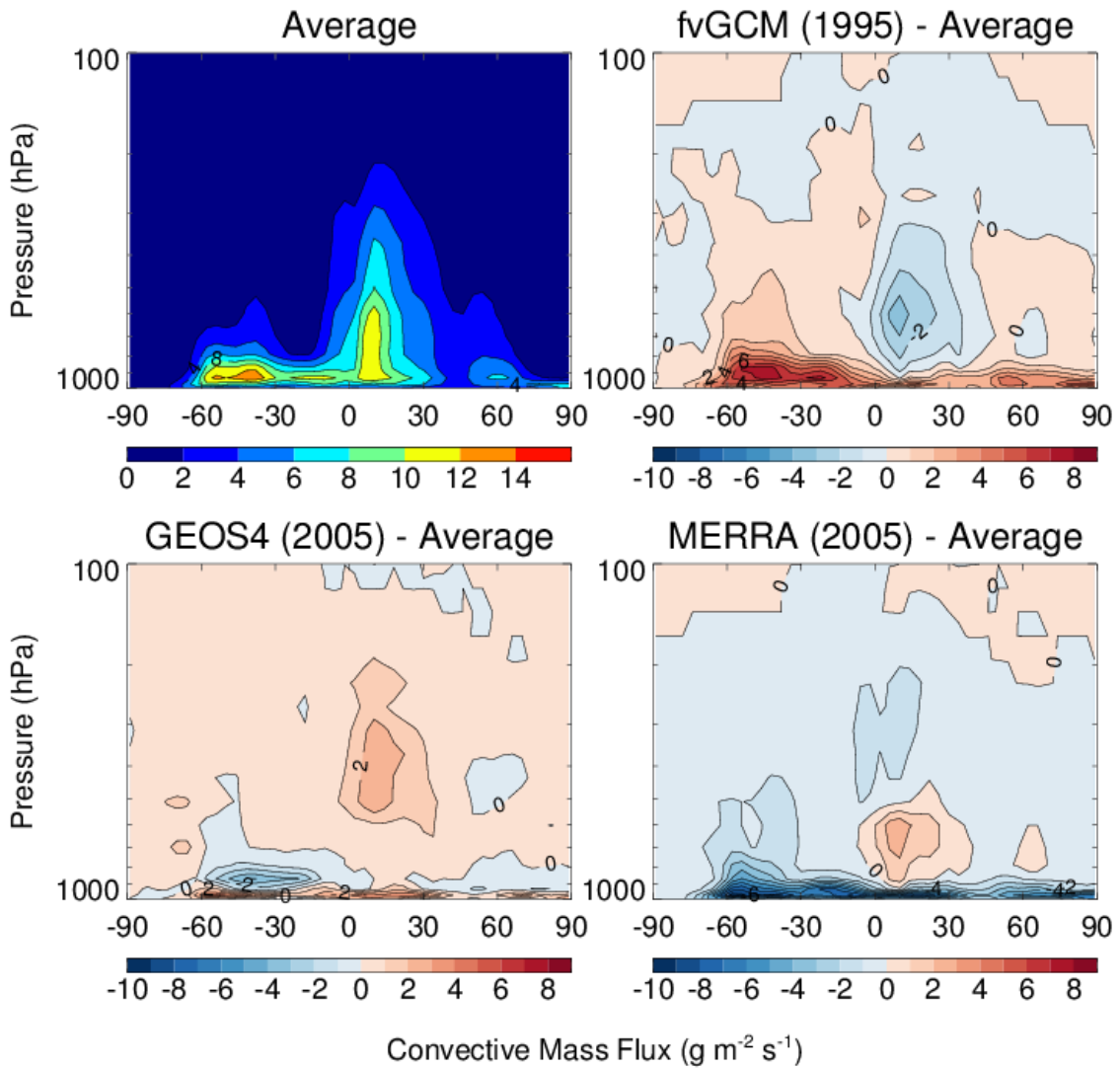
Fig. 1. Latitude-height cross sections of zonal mean convective mass fluxes during July-August.
The plot shows the values averaged over the fvGCM (1995), GEOS4 (2005), and MERRA (2005)
meteorological data sets, as well as differences from the average.
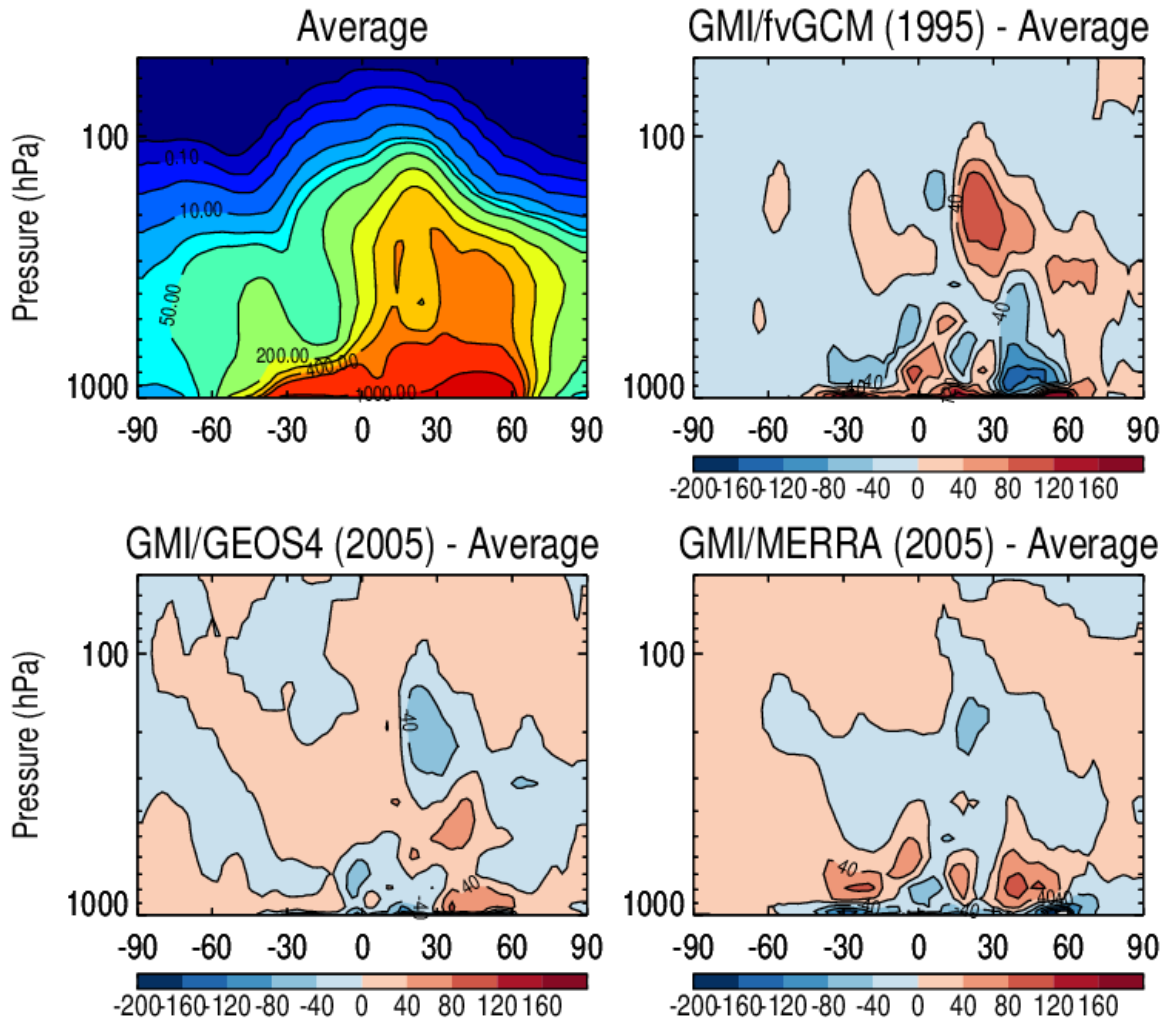
3
4   **Fig. 2.** Latitude-height cross sections of zonal mean ^{222}Rn concentrations (mBq SCM^{-1}) as
5   simulated by GMI for July-August. The plot shows the values averaged over three simulations
6   driven by the fvGCM (1995), GEOS4 (2005), and MERRA (2005) meteorological data sets, as
7   well as differences of each simulation from the average.
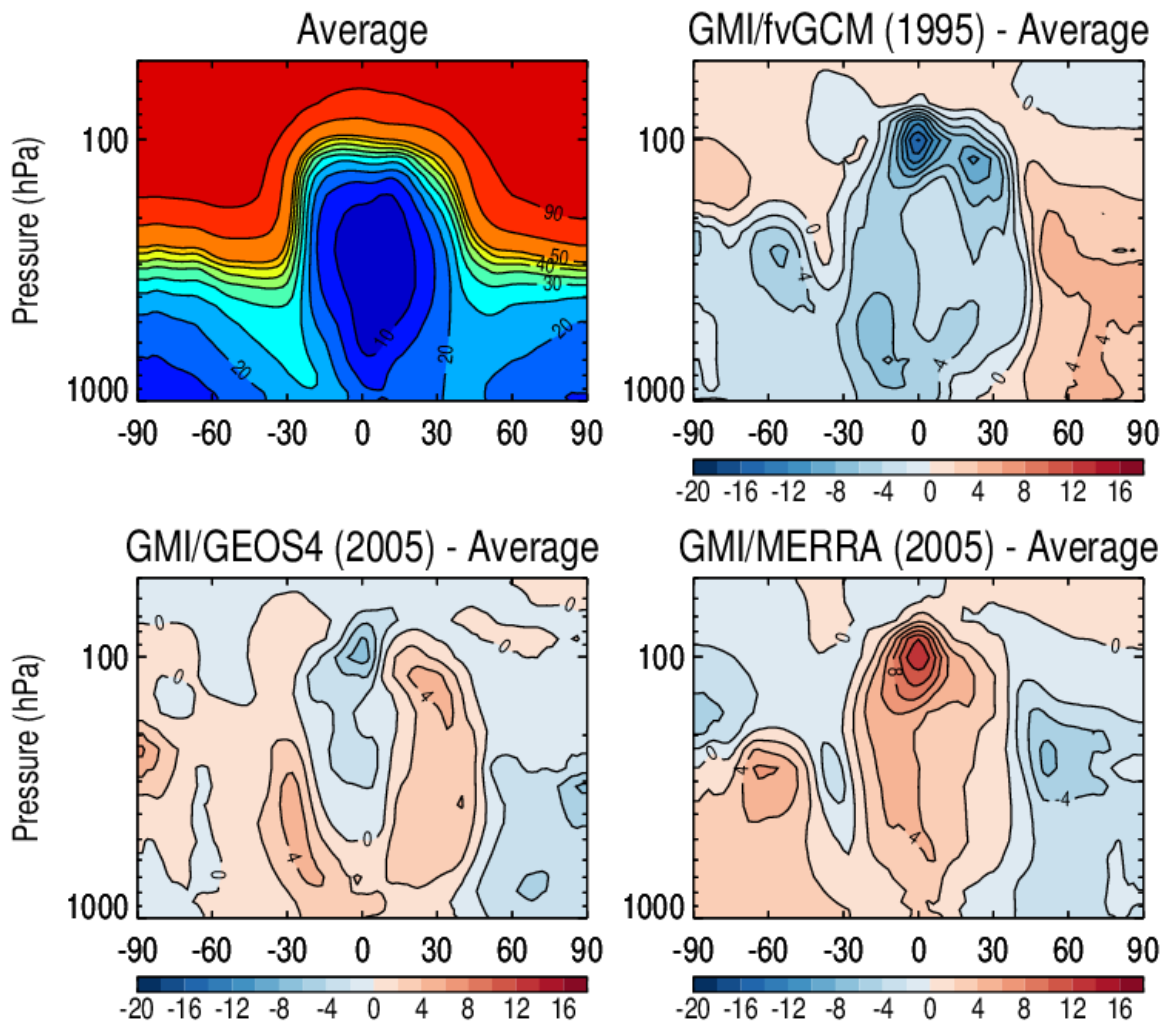
Fig. 3. Same as Fig. 2, but for stratospheric fraction (%) of zonal mean tropospheric [7]Be
concentrations.
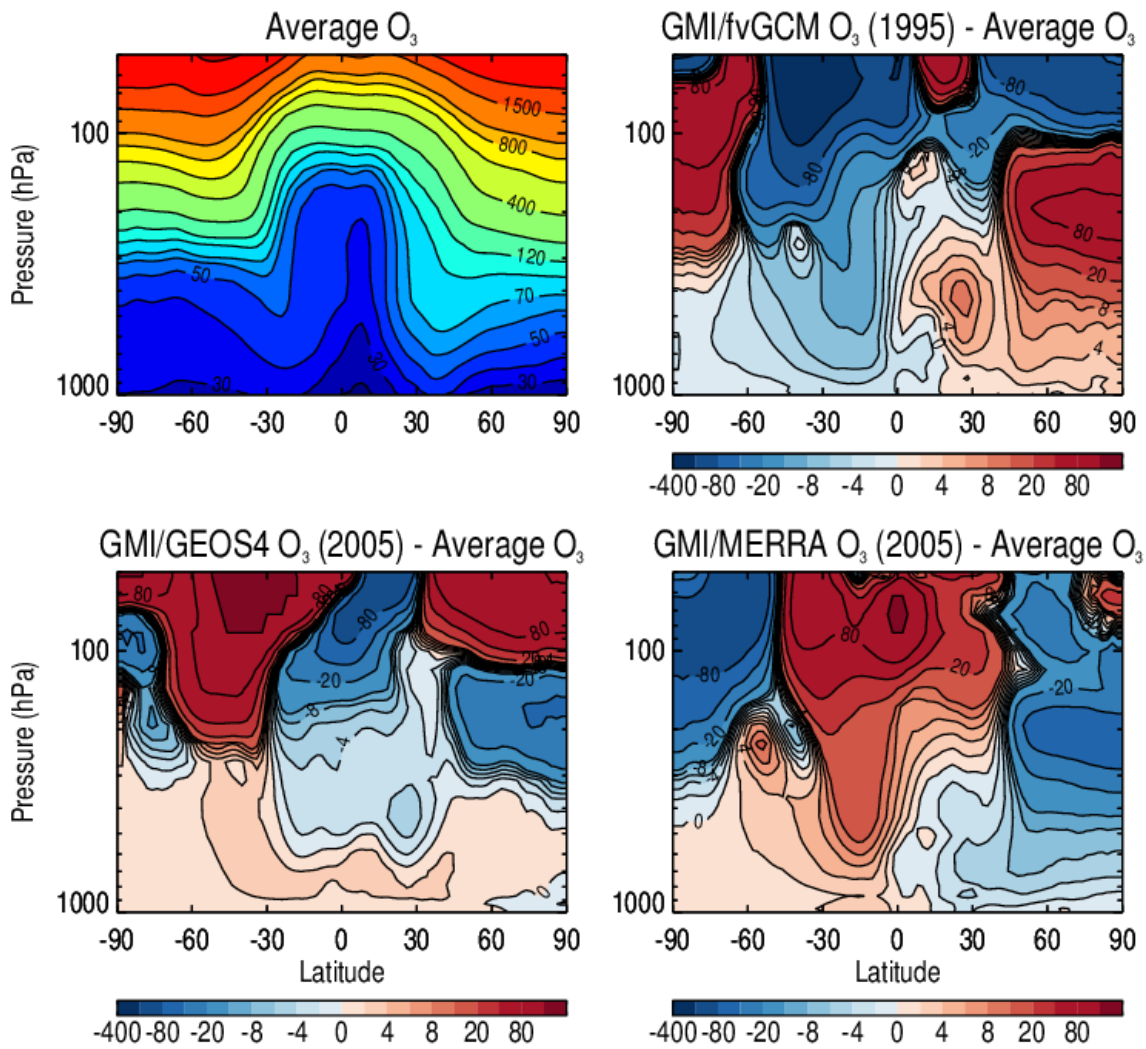
Fig. 4. Same as Fig. 2, but for zonal mean ozone mixing ratios (ppbv).
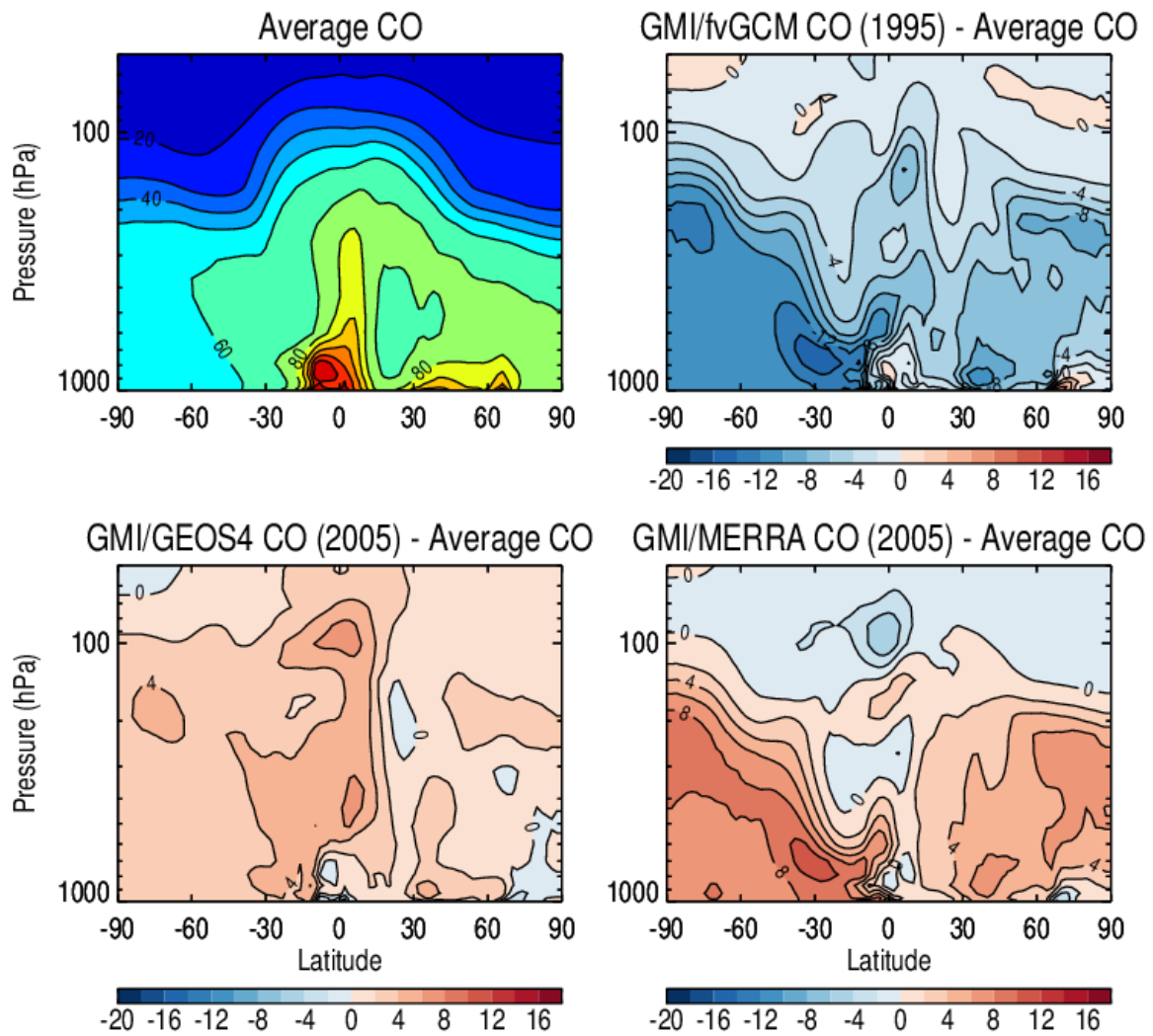
4   **Fig. 5**. Same as Fig. 2, but for zonal mean CO mixing ratios (ppbv).
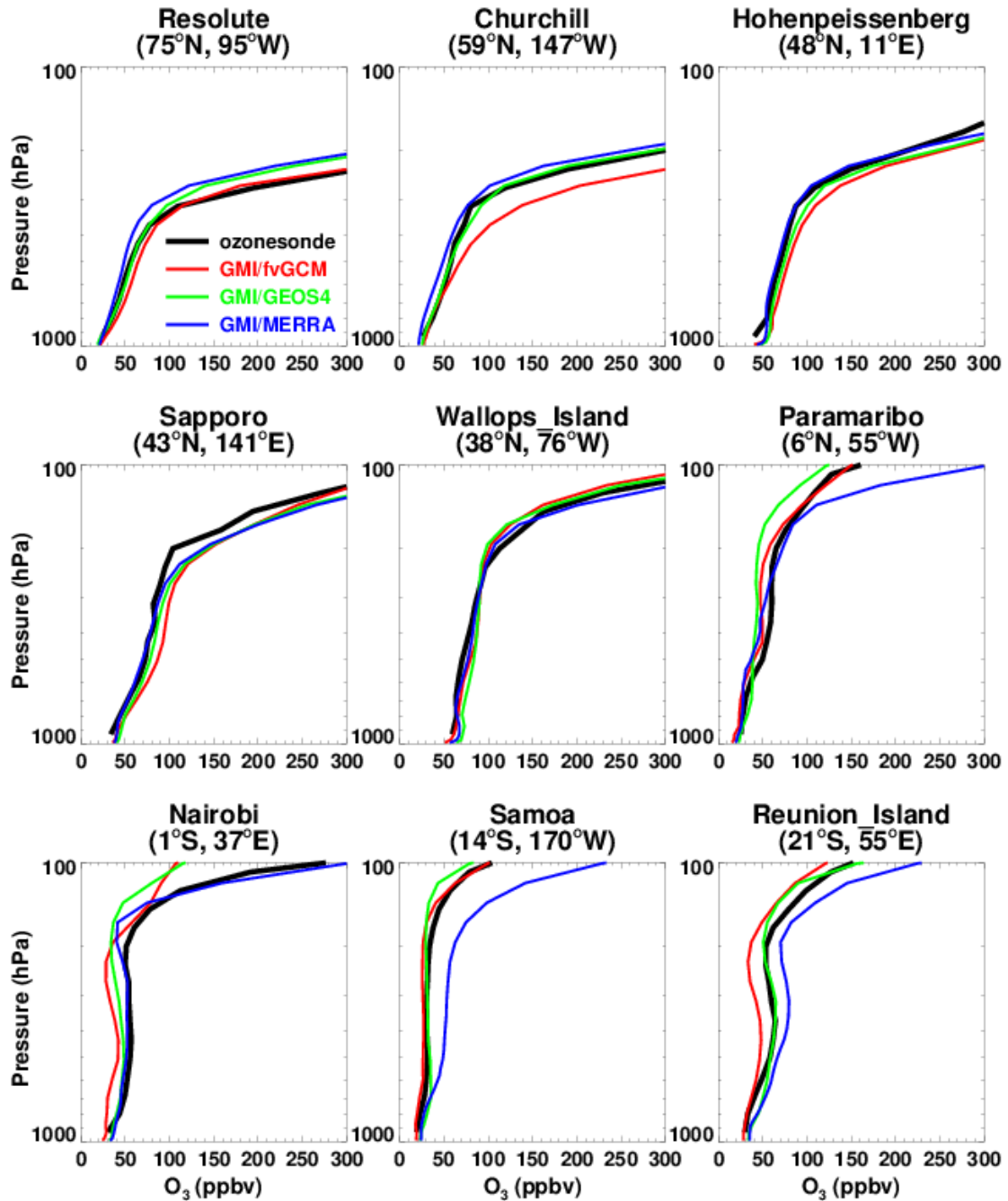
3 **Fig. 6.** Comparisons of GMI simulated tropospheric ozone profiles (color lines) with ozonesonde
4 observations (black line) for a range of latitudes. The model is driven by the fvGCM, GEOS4, and
5 MERRA meteorological fields. Values are July–August average.
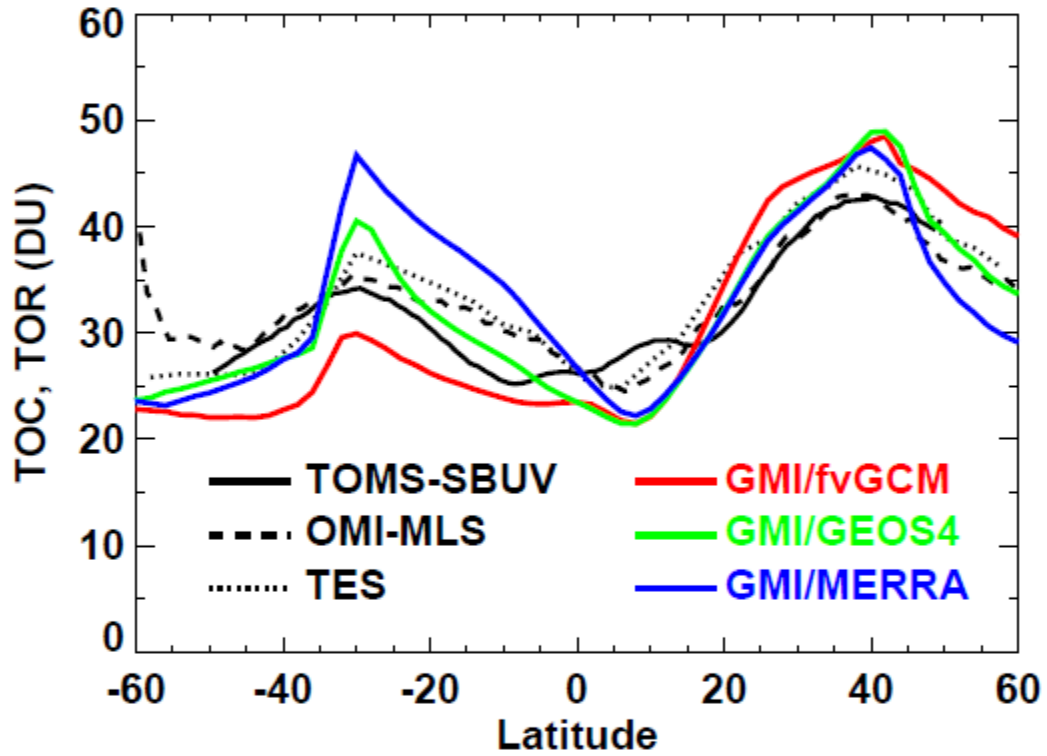
3 **Fig. 7.** GMI simulated zonal mean tropospheric ozone columns (TOCs) compared with
4 tropospheric ozone residuals (TORs) determined from TOMS/SBUV (July–August 1979-2005
5 multi-year average) (Fishman et al., 2003), OMI/MLS (July–August 2005 average) (Ziemke et al.,
6 2006), and TOCs determined from TES retrievals (July–August 2005 average).
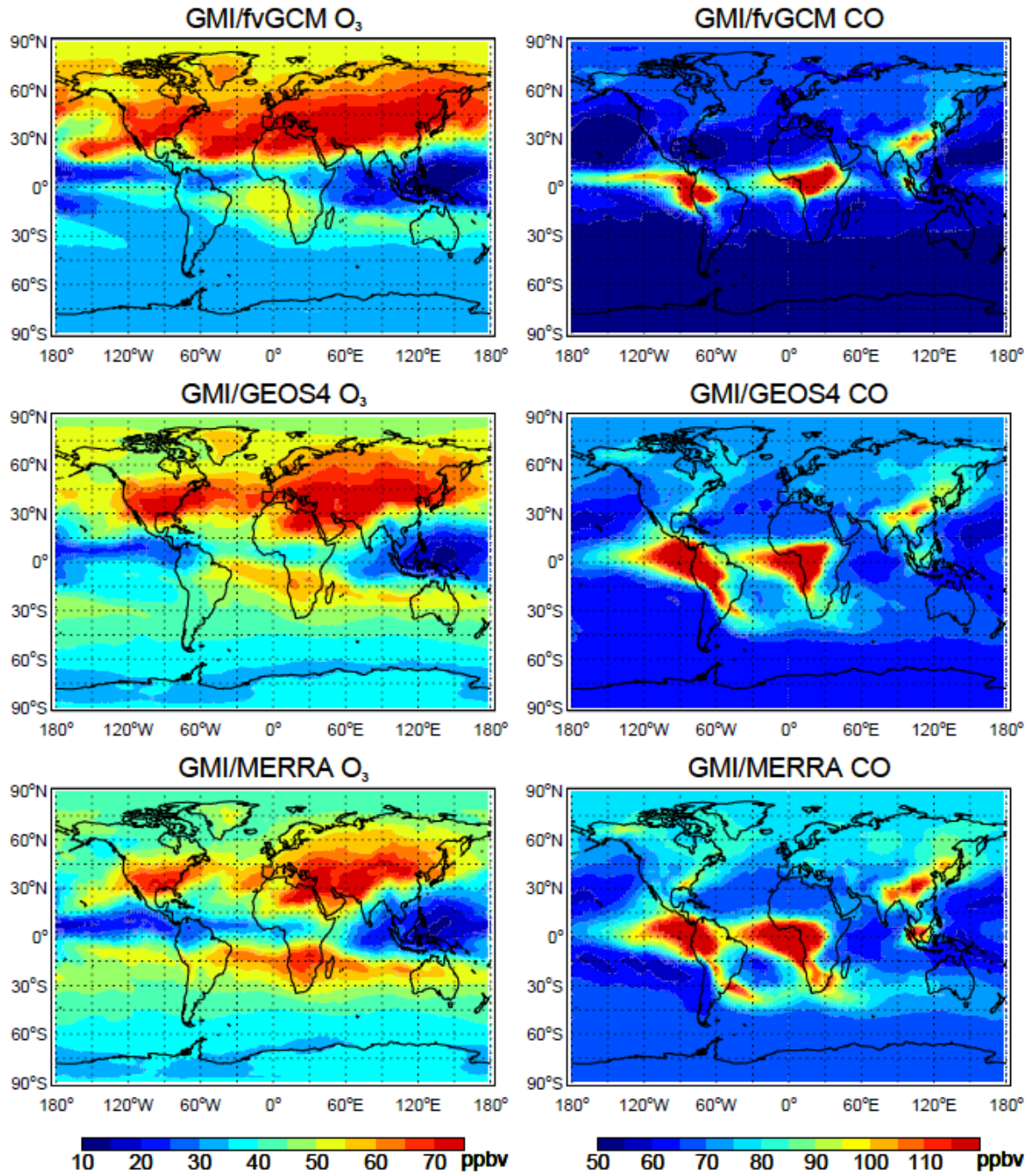
Fig. 8. July-August mean mixing ratios of O_3 and CO (ppbv) at 618 hPa as simulated by GMI CTM driven by three meteorological datasets (1995 for fvGCM, 2005 for GEOS4 and MERRA).
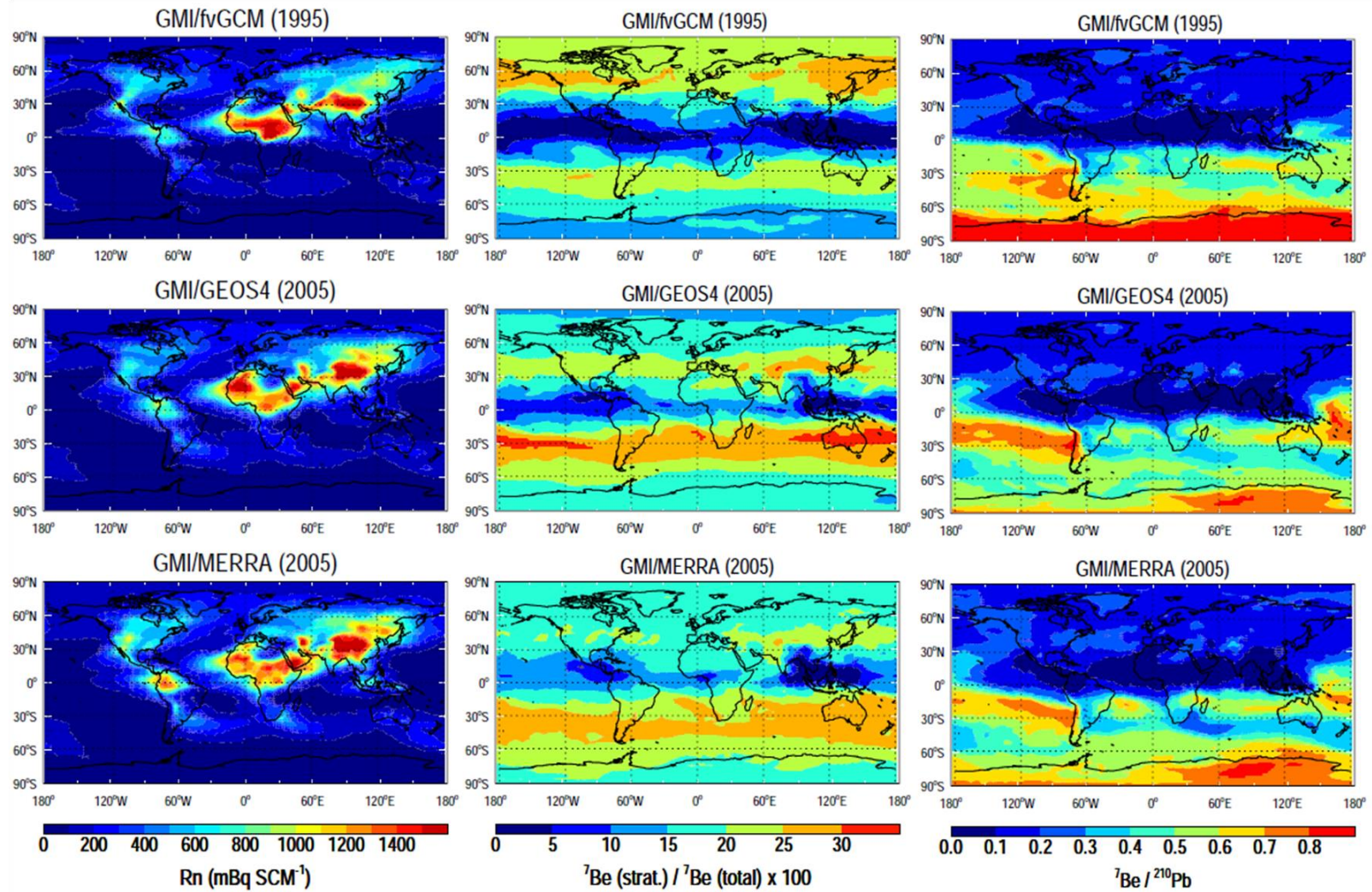
Fig. 9. Mean ^{222}Rn concentrations (mBq SCM^{-1}) (left column), stratospheric fraction (%) of tropospheric ^{7}Be concentrations (middle column), and ratios of ^{7}Be to ^{210}Pb volume mixing ratios (right column) at 618 hPa in the GMI model driven by the fvGCM (1995), GEOS4 (2005), and MERRA (2005) meteorological data sets for the period of July - August.
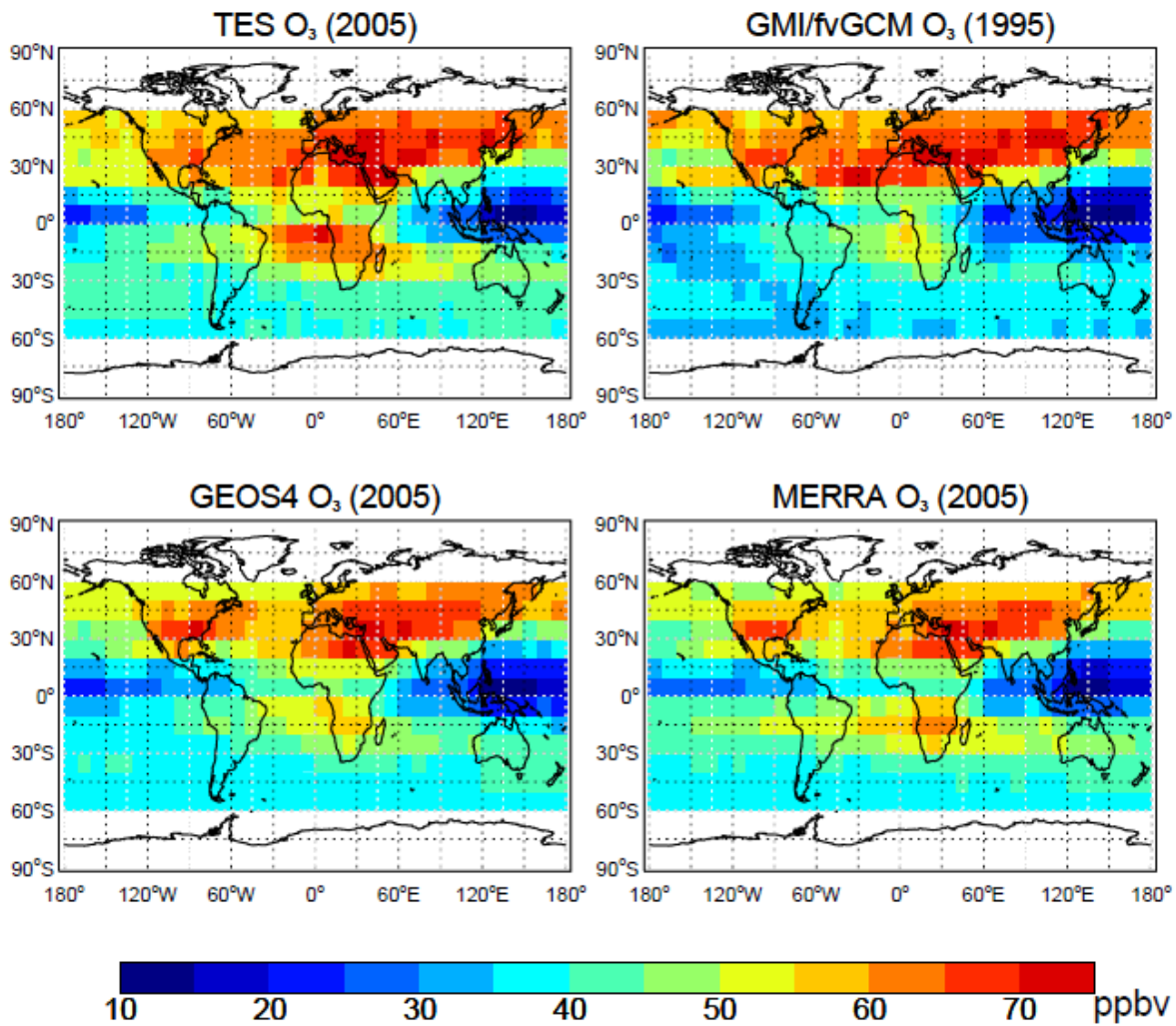
6 **Fig. 10.** Mean mixing ratios of O₃ at 618 hPa observed by TES during July- August 2005 and
7 corresponding GMI CTM results with 3-hourly output sampled along the TES orbit tracks. TES
8 averaging kernels and *a priori* were applied to the model output. Results are averaged into 10°×10°
9 grid cells.
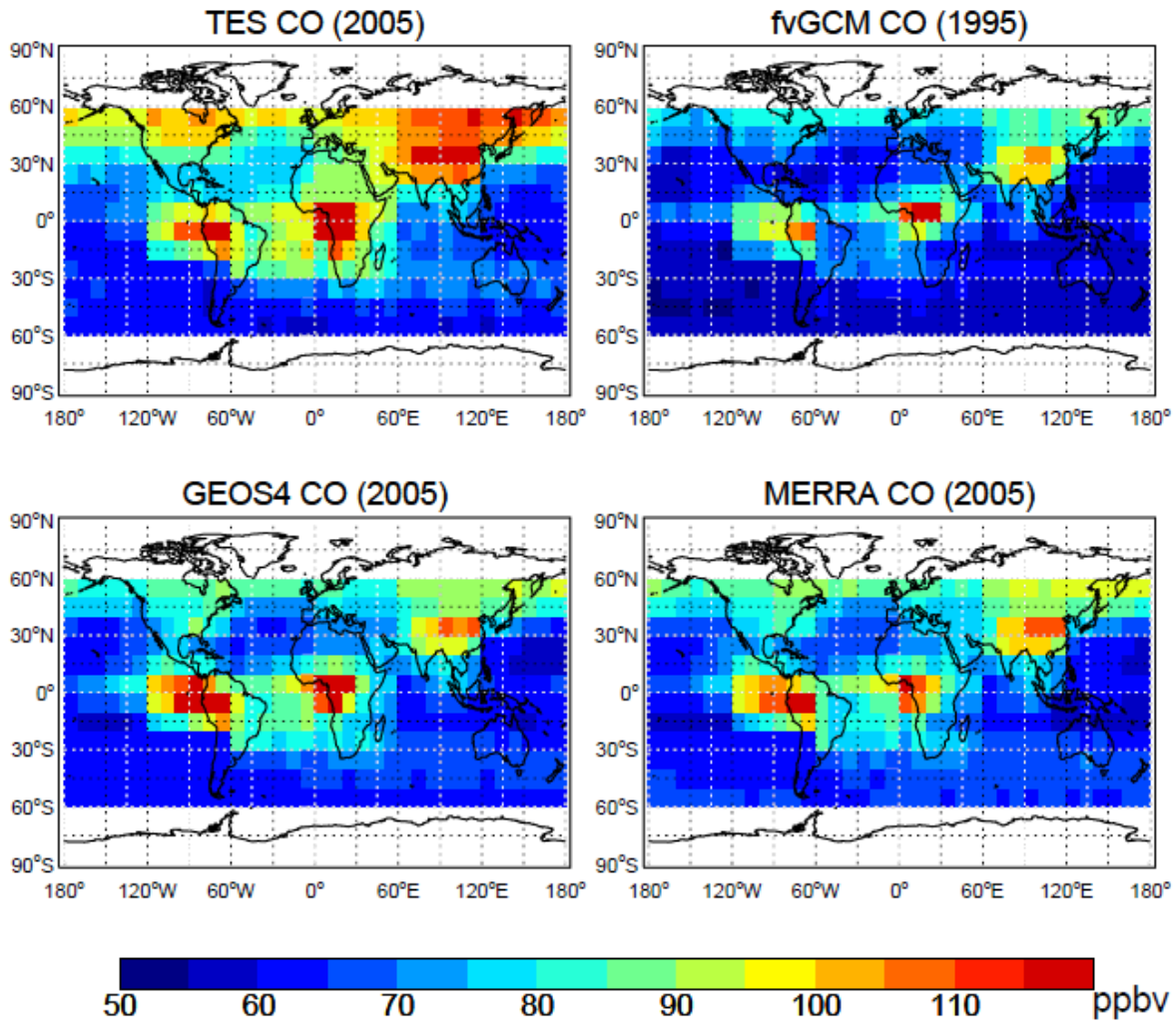
7   **Fig. 11.** Same as Fig. 10, but for CO.
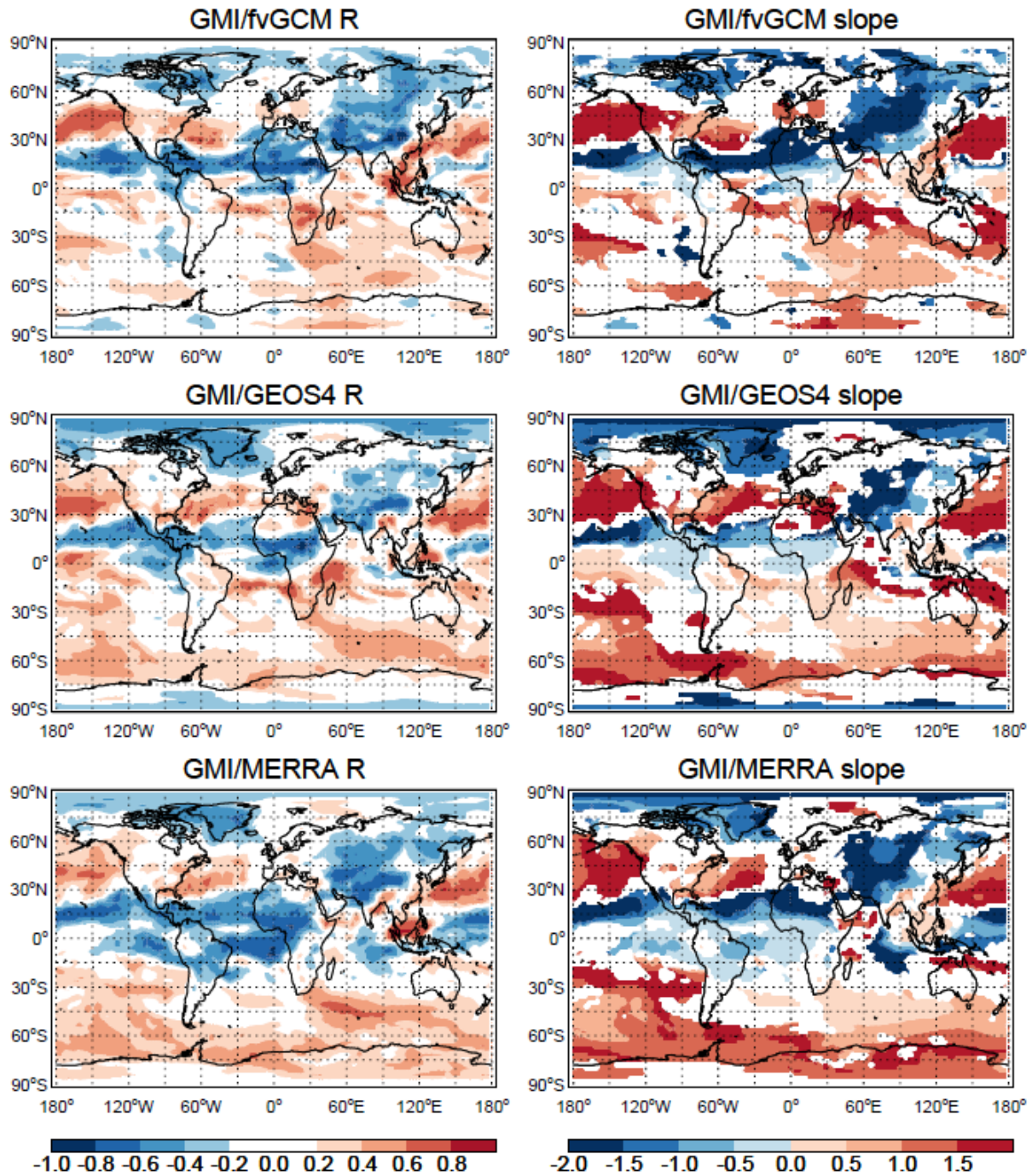
Fig. 12. O$_3$-CO correlation coefficients (R) and linear regression slopes (dO$_3$/dCO) at 618 hPa in the GMI model driven by the fvGCM (1995), GEOS4 (2005), and MERRA (2005) meteorological fields. Results are calculated in 2°×2.5° grid cells using 3-hourly model output and the reduced major axis method. White areas denote absolute values of O$_3$-CO correlation coefficients less than 0.2.
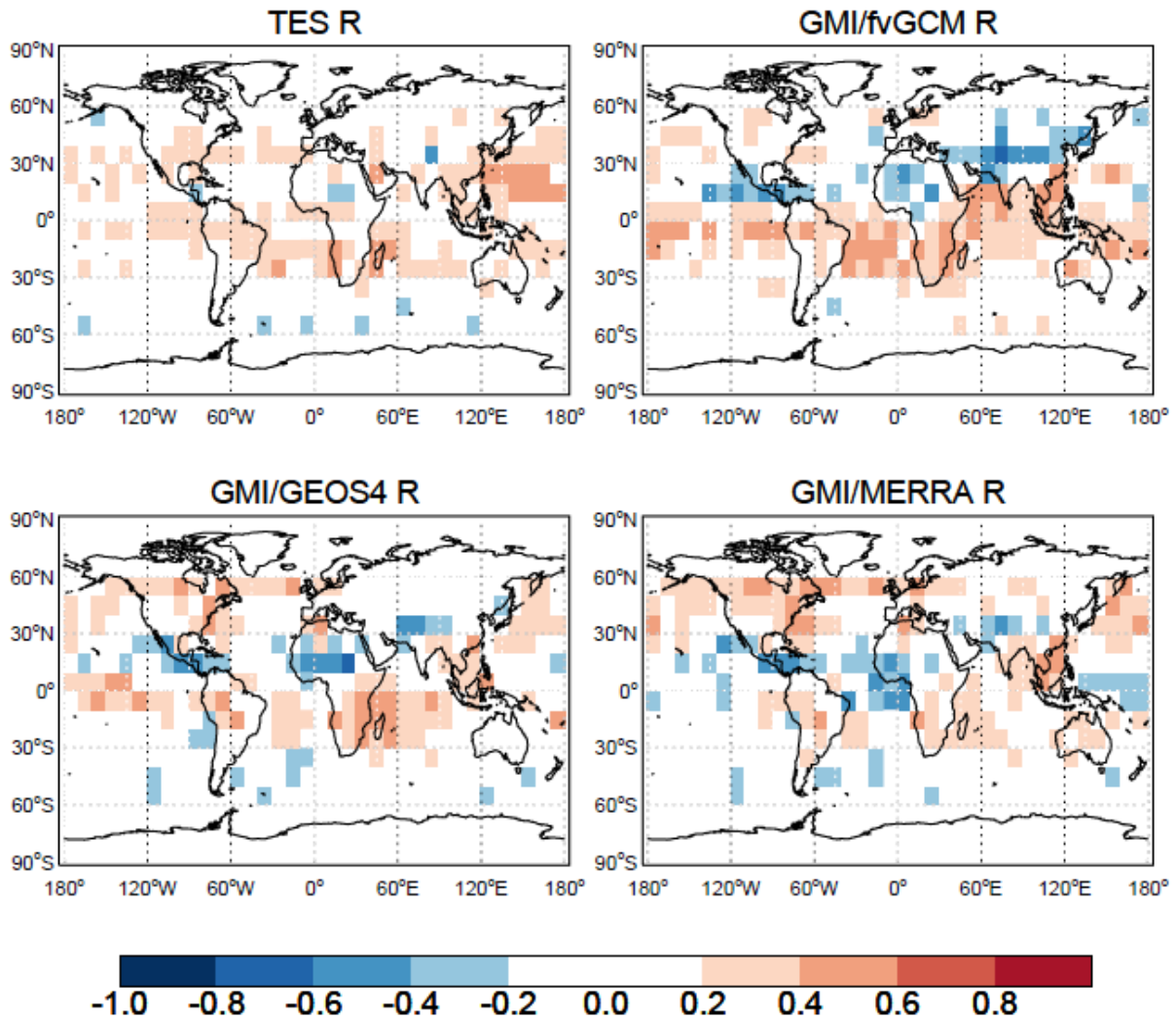
Fig. 13. O_3-CO correlation coefficients (R) at 618 hPa as determined by O_3 and CO observations from TES during July – August 2005, and corresponding GMI CTM results with 3-hourly output sampled along the TES orbit tracks. TES averaging kernels, spectral errors, and a priori are applied. Results are calculated in $10° \times 10°$ grid cells. White areas denote absolute values of O_3-CO correlation coefficients less than 0.2.
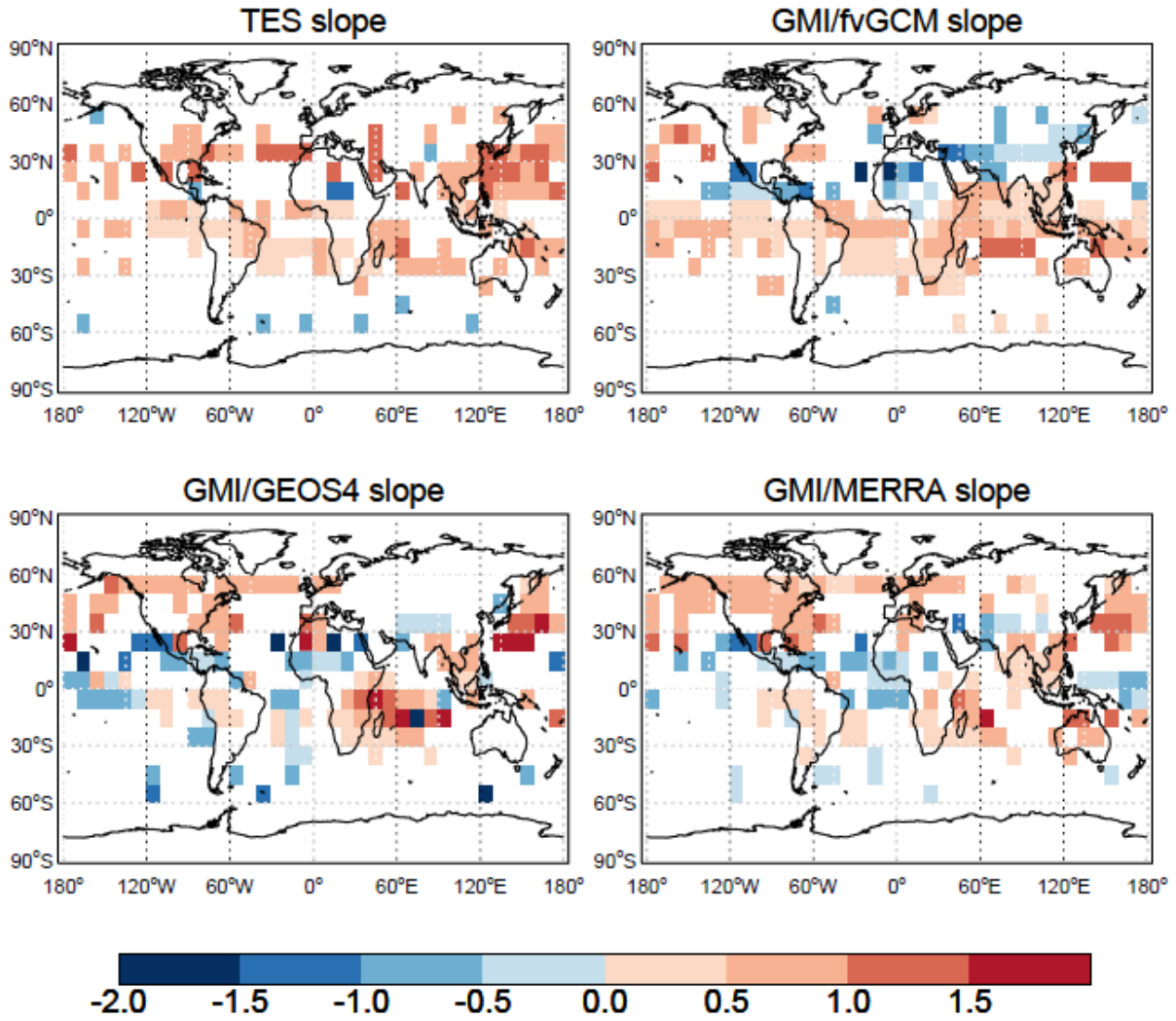
Fig. 14. Same as Fig. 13, but for linear regression slopes dO_3/dCO.
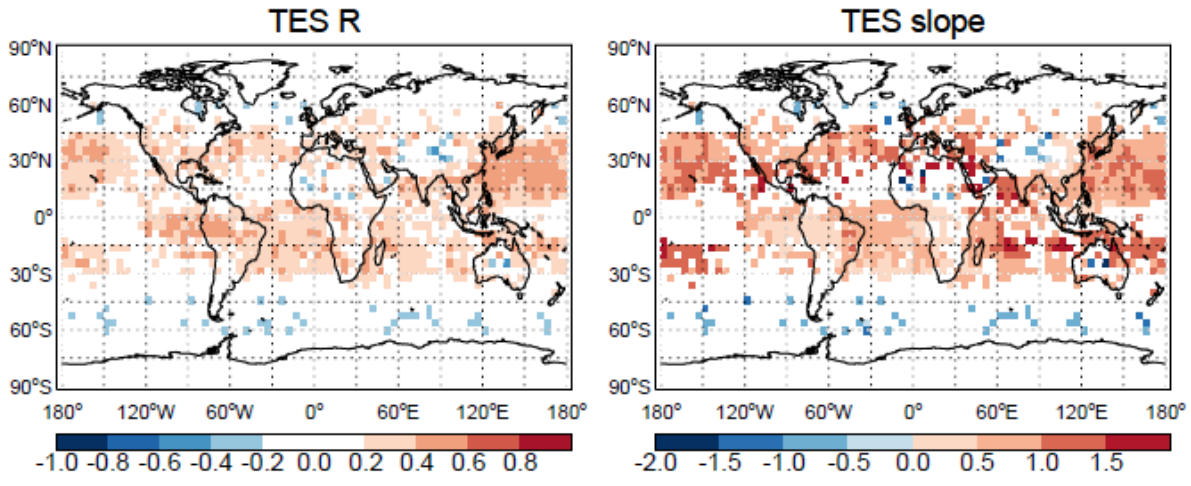
Fig. 15. O_3-CO correlation coefficients (R) and linear regression slopes (dO_3/dCO) at 618 hPa as determined by O_3 and CO observations from TES during July–August, 2005 – 2009. Results are calculated in $4°\times5°$ grid cells. White areas denote absolute values of O_3-CO correlation coefficients less than 0.2.
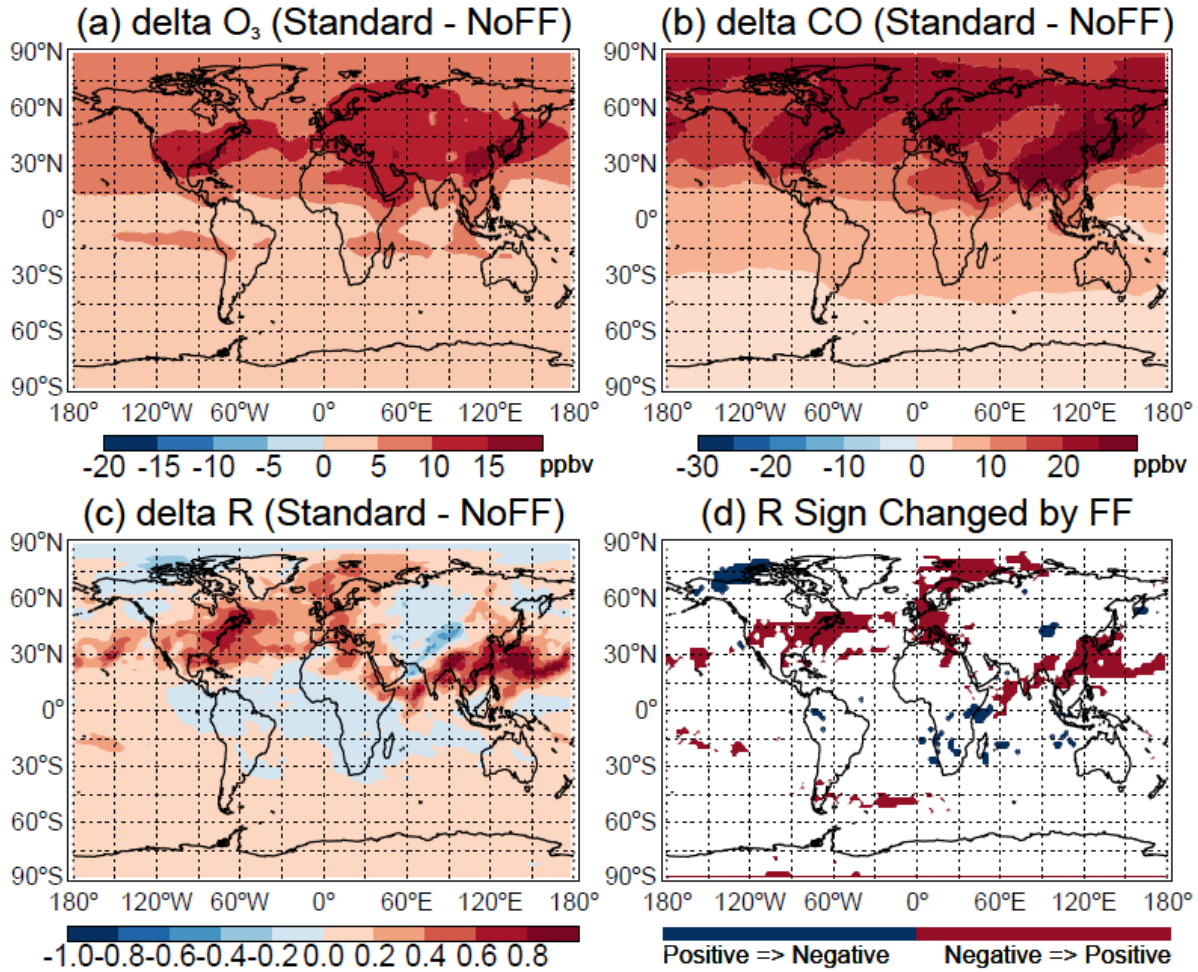
Fig. 16. Sensitivity of O₃, CO, and their correlations to fossil fuel (FF) emissions during July – August 2005. The plots show the mean differences in (a) O₃, (b) CO mixing ratios (ppbv), and (c) O₃-CO correlation coefficients (R) at 618 hPa between the standard GMI/MERRA simulation and a simulation where fossil fuel emissions are suppressed (NoFF) in the model. Also shown in (d) are the areas with changed correlation signs. Results are calculated using 3-hourly model output.
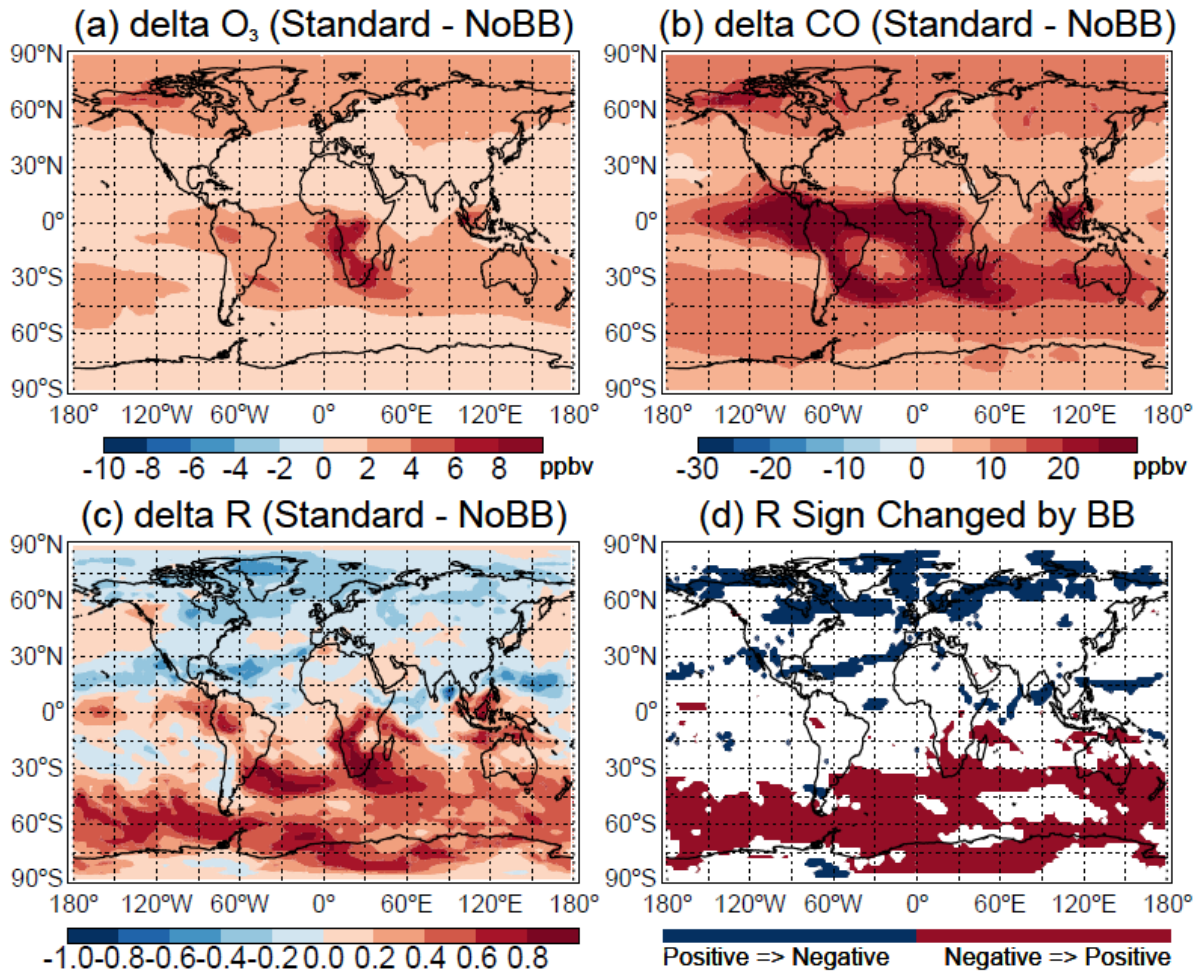
Fig. 17. Same as **Fig. 16**, but for the sensitivity of O_3, CO, and their correlations at 618 hPa to biomass burning (BB) emissions.
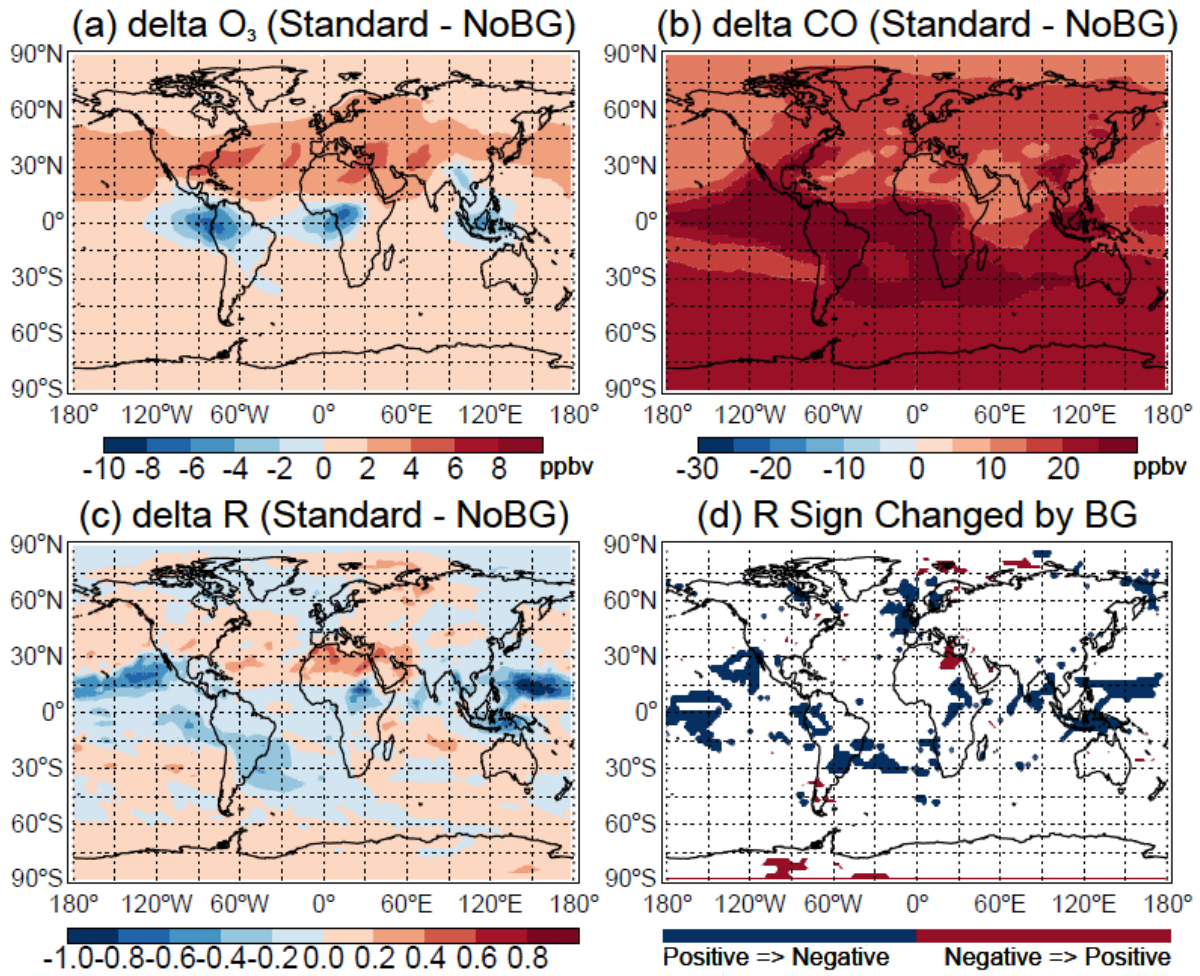
Fig. 18. Same as **Fig. 16**, but for the sensitivity of O₃, CO, and their correlations at 618 hPa to biogenic (BG) emissions.
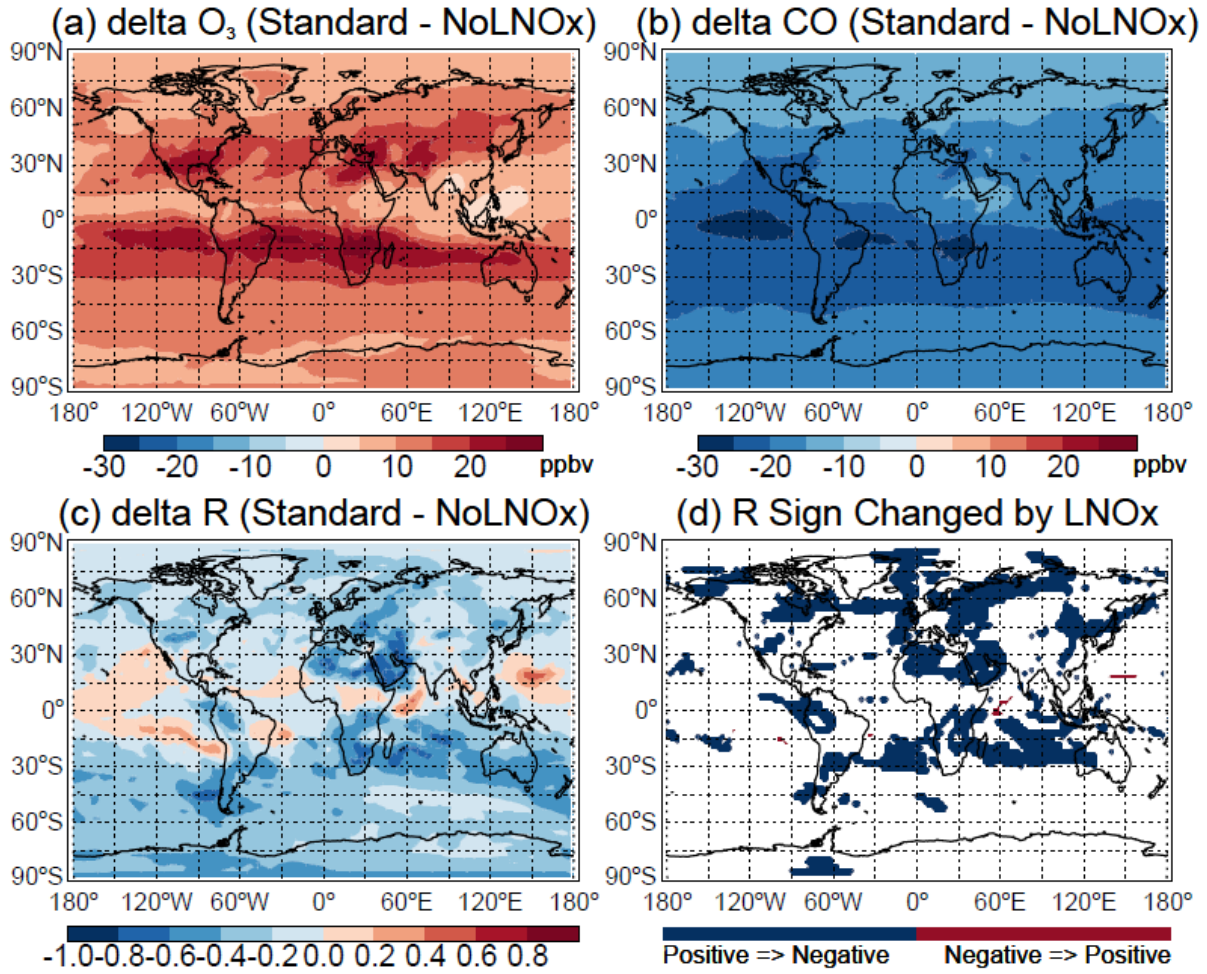
4   **Fig. 19.** Same as **Fig. 16**, but for the sensitivity of O_3, CO, and their correlations at 618 hPa to
5   lightning NO_X (LNO_X) emissions.
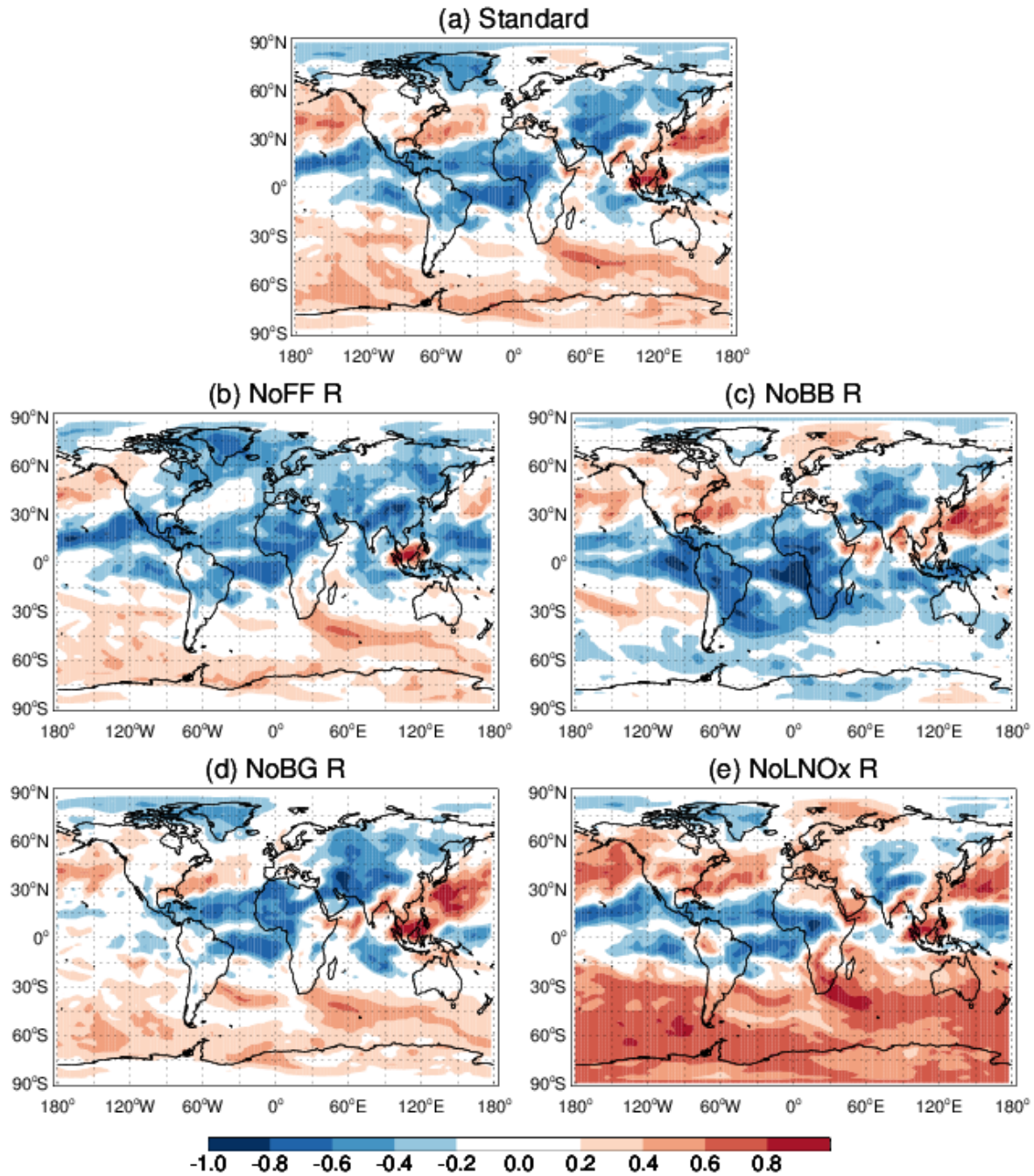
Fig. 20. GMI/MERRA-simulated O_3-CO correlations (R) at 618 hPa (a) in the standard simulation and (b) - (e) when fossil fuel (FF), biomass burning (BB), biogenic (BG), and lightning NOx (LNO$_X$) emissions are individually suppressed (NoFF, NoBB, NoBG, and NoLNO$_X$, respectively) in the model during July-August 2005. Results are calculated using 3-hourly model output. White areas denote absolute values of O_3-CO correlation coefficients less than 0.2.